Ab initio calculations
of the optical properties
# of phase-change materials

Manfred Niesert

Version: August 11, 2003

Contents

Chapter 1

Introduction

Chapter 2

Density Functional Theory

2.1 The Many-Particle Problem

The complete properties of solids can in principle be calculated *ab initio* – i.e. free of any parameters, only using the setup of the system and its interactions – on a quantum mechanical level. The whole information of a system is contained in the system's wave-function, which has to be obtained as solution of the Schrödinger equation

$$\mathcal{H}|\Psi\rangle = E|\Psi\rangle, \tag{2.1}$$

with $\mathcal{H}$ the Hamiltonian of a system of interacting nuclei and electrons (assuming $4\pi\varepsilon_0 = 1$)

$$\mathcal{H} = -\sum_{i=1}^{N} \frac{\hbar^2}{2m}\nabla_i^2 + \frac{1}{2}\sum_{i\neq j} \frac{e^2}{|\mathbf{r}_i - \mathbf{r}_j|} - \sum_{i,J} \frac{Z_J e^2}{|\mathbf{r}_i - \tau_J|} + \frac{1}{2}\sum_{I\neq J} \frac{Z_I Z_J e^2}{|\tau_I - \tau_J|}. \tag{2.2}$$

$\mathbf{r}$ denote the electronical coordinates and τ those of the nuclei, Z_I denotes the charge of the nuclei. Spin-dependence and external fields are omitted. In the relativistic case, the Dirac equation has to be solved. The energy of a state Ψ is given by

$$E = \langle\Psi|\mathcal{H}|\Psi\rangle. \tag{2.3}$$

The effort to solve this many-body problem scales exponentially with the number of particles described and is unaccomplishable for everything except *very* small systems, and certainly for a macroscopic system with a number of particles of an order of magnitude of 10^{23}.

A first and very general approximation is the Born-Oppenheimer method (also called adiabatic approximation). Since the mass of the electrons is at least three orders of magnitude smaller than those of the nuclei, the electrons are expected to follow the motions of the nuclei instantaneously, while the nuclei will react slowly to a change in electronic configuration. Therefore, the ion's position can be set fixed, reducing the number of degrees of freedom. (From a strict point of view this approximation needs more precise justification, see [Mad78].) This approximation is used in the majority of electronic calculations.

When calculating the ground state of a system, the energy has to take its minimum. Depending on your ansatz, the solution can usually be obtained by minimizing the total energy.

2.2 The Hartree-Fock Ansatz

A variety of different approaches have been developed to tackle this many-particle problem. One frequently used method (in many areas of physics) is to transfer the many-body problem to a *one-particle-like* problem, for instance by imposing some certain form on the wavefunction.

The most basic choice is the *Hartree Ansatz*, which replaces the wavefunction $\Psi(\mathbf{r}_1, \ldots, \mathbf{r}_N)$ with a product of N one-particle wavefunctions $\psi(\mathbf{r})$:

$$\Psi(\mathbf{r}_1, \ldots, \mathbf{r}_N) = \psi_1(\mathbf{r}_1) \cdot \psi_2(\mathbf{r}_2) \cdot \ldots \cdot \psi_N(\mathbf{r}_N), \tag{2.4}$$

depending only on the spatial coordinate of one particle. If one introduces this ansatz into the Schrödinger equation, one obtains N Schödinger-like single-particle equations with a integral called Coulomb term or *Hartree* term, containing the electron-electron interaction. This simple ansatz treats the particles independent in the sense that every particle moves in a static potential created by the other electrons, which is the only interaction considered.

It is possible to take care about the expelling properties of fermions resulting from the Fermi principle – called *exchange* interaction – by using a slater determinant of wavefunctions instead of a simple product:

$$\Psi(\mathbf{r}_1, \ldots, \mathbf{r}_N) = \frac{1}{\sqrt{N}} \begin{vmatrix} \psi_1(\mathbf{r}_1) & \ldots & \psi_N(\mathbf{r}_1) \\ \vdots & \ddots & \vdots \\ \psi_1(\mathbf{r}_N) & \ldots & \psi_N(\mathbf{r}_N) \end{vmatrix} . \tag{2.5}$$

This *Hartree-Fock* Ansatz results in a significantly more complex numerical treatment as well as in much better results. Including a wavefunction of this form into the Schrödinger equation gives N single particle equations now containing an additional term – the *exchange* or *Fock* term – containing contributions from all the other single-particle wavefunctions.

The description is still incomplete due to the fact that the single particles are not independent as assumed in this approximation. These *correlation* effects can not be expressed analytically in the general case.

2.3 Density Functional Theory

A new idea how to describe the ground state of a many-particle system has been acquired by Hohenberg and Kohn in the 1960s. It turns the focus from the abstract many-particle state as descriptive quantity of the system to the ostensive charge density in real space. Not only that not the whole information content of the wave-function is needed, it is not desirable to obtain the complete solution Ψ for a large system since storage of it is as hardly possible as calculation of it.

One different approach, the Thomas-Fermi theory, was known since the late twenties [Fer27, Tho27]. It assumes the interacting electrons to be independent, moving in an external potential. (In this context the term *external* means everything except of this one particle itself, so it includes also the effects of the nuclei in the system, not only those of fields external to the system.) Then the formulae for the uniform electron gas are applied. The obtained results give only a few quantitative trends, chemicals bonds for instance can not be predicted. However, the system is described by the density only.

The Lemma of Hohenberg and Kohn: The charge density relates to the many-particle wavefunction like

$$n(\mathbf{r}) = \left\langle \Psi | \sum_{i=1}^{N} \delta(\mathbf{r} - \mathbf{r}_i) | \Psi \right\rangle. \tag{2.6}$$

The amount of charge

$$N = \int d^3r \; n(\mathbf{r}) \tag{2.7}$$

takes the role of a subsidiary parameter.

Hohenberg and Kohn derived that the expectation value of any observable is uniquely defined by the charge density. Furthermore, the functional of total energy

$$E = E[n(\mathbf{r})] \tag{2.8}$$

is minimized by the true ground state density $n_0(\mathbf{r})$. As a third point, the

The important conclusion of the Lemma of Hohenberg and Kohn [HK64] is that the density $n(\mathbf{r})$ of the ground state of a system of interacting electrons in some external potential $v(\mathbf{r})$ determines this potential uniquely (of course up to some unimportant constant). The proof is shown in contradiction for the energy functional

$$E_g = \langle \Psi_g | \mathcal{H} | \Psi_g \rangle \tag{2.9}$$

of a non-degenerate ground state, which is shown to be expressable in terms of the density,

$$E_g = E[n(\mathbf{r})]. \tag{2.10}$$

It is shown that It can easily be extended to the degenerate case [Koh85].

This means that $n(\mathbf{r})$, determining the potential $v(\mathbf{r})$ and the number of particles N, describes the Hamiltonian and therewith the complete system and all its derivable properties (including many-body wavefunctions, two-particle Green's functions). A more mathematical insight is that there are functions $n(\mathbf{r})$ not yielding a valid potential $v(\mathbf{r})$, so-called non V-representable functions. These are non-physical densities.

The Hohenberg-Kohn lemma does not imply any knowledge about the physical interactions and is universal thereby. On the other hand, nothing has been stated about the form of the functional $E[n]$ up to now.

Kohn-Sham equations: Kohn and Sham formulated a form for the energy functional that proved to be very successful. They proposed to split it up into three contributions

$$E[n] = T_s[n] + U[n] + E_{xc}[n]. \tag{2.11}$$

T_s is the kinetic energy of *non-interacting* particles, U is the Coulomb energy, and E_{xc} contains the remaining contributions to the energy due to exchange and correlation. The Coulomb energy of the electrons is constructed out of the electron-electron energy together with the external energy, resulting additively from the Coulomb field of the nuclei and from fields external to the system:

$$\begin{aligned} U[n] &= E_{ext}[n] + E_H[n] && (2.12) \\ E_{ext}[n] &= \int d^3r \ V_{ext}(\mathbf{r}) n(\mathbf{r}) && (2.13) \\ E_H[n] &= \frac{e^2}{8\pi\varepsilon_0} \int d^3r d^3r' \ \frac{n(\mathbf{r})n(\mathbf{r}')}{|\mathbf{r}-\mathbf{r}'|} && (2.14) \end{aligned}$$

An advantage of this representation is that for the kinetic energy, which is a significant proportion to the total energy, an analytic expression can be given (see section 2.7). The density is related to the single particle wavefunctions via

$$n(\mathbf{r}) = 2\sum_{i=1}^{N} |\psi_i(\mathbf{r})|^2, \tag{2.15}$$

with the factor 2 accounting the spin degeneracy[1]. For this choice the kinetic energy reads

$$T_s[n] = -2\sum_{i=1}^{N} \int d^3r \ \psi_i^*(\mathbf{r}) \frac{\hbar}{2m} \nabla^2 \psi_i(\mathbf{r}). \tag{2.16}$$

---

[1] In this case, you calculate with half the number of electrons

Equivalent to minimizing the energy with respect to the density, one can do so as well with respect to the single wavefunctions or to their complex conjugates. The subsidiary condition of particle conservation (2.7) is replaced by the normalization of the wavefunctions

$$\int d^3r \; |\psi_i(\mathbf{r})|^2 = 1. \tag{2.17}$$

Taking this requirement into account by Lagrange parameters ϵ_i, the variation of the energy yields the *Kohn-Sham equations*

$$\mathcal{H}_1\psi_i(\mathbf{r}) = \left\{ -\frac{\hbar}{2m}\nabla^2 + V_{eff}(\mathbf{r}) \right\} \psi_i(\mathbf{r}) = \epsilon_i\psi_i(\mathbf{r}), \tag{2.18}$$

which are Schrödinger-like equations of a one-particle Hamiltonian $\mathcal{H}_1$ containing an effective potential

$$V_{eff}(\mathbf{r}) = V_{ext}(\mathbf{r}) + V_H(\mathbf{r}) + V_{xc}(\mathbf{r}) \tag{2.19}$$

consisting of the external, the Hartree and the exchange-correlation potential

$$\begin{aligned} V_{ext}(\mathbf{r}) &= \frac{\delta}{\delta n(\mathbf{r})} E_{ext}(\mathbf{r}) && (2.20) \\ V_H(\mathbf{r}) &= 4\pi e^2 \int d^3r \frac{n(\mathbf{r}')}{|\mathbf{r} - \mathbf{r}'|} && (2.21) \\ V_{xc}(\mathbf{r}) &= \frac{\delta}{\delta n(\mathbf{r})} E_{xc}(\mathbf{r}). && (2.22) \end{aligned}$$

These potentials are simple functions, while the corresponding energies are considered as functionals of the density.

This choice (2.11) of kinetic energy and subsequent derivations converts the problem to a problem of fictitious single particles moving in an effective potential all other particles contribute to.

The parameter ϵ_i are introduced as Lagrangian parameters only. According to Janak's theorem, only the highest occupied value has a physical meaning, i.e. it is equal to the chemical potential, the ionisation energy of the system. Beyond this, there is no justification to take these parameters as the one-particle energies. However, it is known from experience that this assumption works surprisingly good, and this identity is commonly assumed in bandstructure calculations.

Eigenvalue problem: Usually the Kohn-Sham equations (2.18) are not solved directly, but the solutions are represented in a basis. Then the operator $\mathcal{H}_1$ has to be constructed and diagonalized. Since the basis functions are not necessarily orthogonal, one has to solve the generalized eigenvalue problem

$$(\mathcal{H}_1 - \epsilon_i\mathcal{S})\mathbf{c} = 0 \tag{2.23}$$

(also called secular equation) with $\mathcal{S}$ the overlap matrix and $\mathbf{c}$ the expansion coefficients.

Self-consistency: Since the electron density goes into the Hartree potential V_H and the exchange-correlation potential V_{xc}, and the effective potential determines the solutions ψ_i through (2.18), which again make the charge density (2.15), this formalism comprises a self-consistency, as shown in figure (2.1).

Figure 2.1: The self-consistency cycle of a density-functional calculation.

To enter the loop one has to provide an appropriate starting density. With this the potentials are generated and the one-particle solutions are calculated. In matrix picture this is the setup of the $\mathcal{H}$ and $\mathcal{S}$ matrices and the solution of the generalized eigenvalue problem (2.23). With the results the temporary density $n_{new}(\mathbf{r})$ is calculated.

One now checks if the difference between the previous density $n^{(i)}(\mathbf{r})$ and the new one is sufficiently small. If not, the temporary density is incorporated into the previous one. Since taking the calculated density as next input density $n^{(i+1)}(\mathbf{r})$ for the cycle would introduce too big steps which destroy convergence, some mixing has to be performed. The simplest way is a linear mixing

$$n^{(i+1)}(\mathbf{r}) = (1-\alpha)n^{(i)}(\mathbf{r}) + \alpha\ n_{new}(\mathbf{r}) \tag{2.24}$$

with mixing parameter α. More sophisticated methods like those of Broyden and Anderson have been developed, which incorporate the knowledge of earlier iterations and yield a faster convergence. After finishing the loop, one can process the obtained density, e.g. calculate the total energy.

2.4 Exchange and Correlation

Since no approximations have been made so far, density functional theory is exact in principle. However, calculations are only possible with the knowledge of the exchange-correlation energy functional $E_{xc}[n]$ defined by (2.11). The exact functional is unknown and not soluble analytically. Solving it would be equivalent to solving the many-body problem. Therefore, approximations have to be made.

Basically, the Kohn-Sham equations are a Hartree-like ansatz. All exchange and correlation effects (i.e. all many-body effects) are included in the functional $E_{xc}[n]$. It contains the fermionic effects, modifications to the effective potential and corrections to the kinetic energy, all due to the electron-electron interaction. This means that the exchange-correlation potential describes the effects of the Pauli principle and the Coulomb potential beyond a pure electrostatic interaction of the electrons.

The most widely used approach is the *Local Density Approximation* (LDA). The idea is to assume E_{xc} to be that of a homogenous electron gas with density $n(\mathbf{r})$:

$$E_{xc}[n(\mathbf{r})] = \int d^3r \; n(\mathbf{r})\epsilon_{xc}(n(\mathbf{r})). \tag{2.25}$$

The important simplification is that ϵ_{xc} is not a functional of the density, but a function of the value of the density at some spatial coordinate. With this, also the exchange-correlation potential V_{xc} in (2.20) takes the form of a function. One possible approximation is to view exchange and correlation to be independent:

$$\epsilon_{xc}(n(\mathbf{r})) = \epsilon_x(n(\mathbf{r})) + \epsilon_c(n(\mathbf{r})) \tag{2.26}$$

More complex parametrisations incorporate the results of Hartree-Fock or many-body calculations. One would expect the LDA to fail systems with rapidly varying densities. But it shows to give good results in an unexpected variety of systems.

A class of more sophisticated approximations is the *Generalized Gradient Approximation* (GGA). It makes the same localization ansatz as in (2.25), but connects ϵ_{xc} not only with the value of the density but also with the absolute value of its gradient:

$$E_{xc}[n(\mathbf{r})] = \int d^3r \; n(\mathbf{r})\epsilon_{xc}(n(\mathbf{r}), |\nabla n(\mathbf{r})|). \tag{2.27}$$

2.5 Notes on Symmetry

Symmetries are operations that transfer a system into itself, so that both systems are indistinguishable. In this context we are interested in symmetry operations in real space. Symmetry operators commute with the Hamiltonian,

$$[(\alpha, \mathcal{T}), \mathcal{H}] = 0. \tag{2.28}$$

$(\alpha, \mathcal{T})$ denotes an operation consisting of a rotation α and a subsequent translation $\mathcal{T}$. Taking symmetries into account can massively simplify the calculations, or makes it only possible.

Classifications: Perfect crystals, that are systems possessing translational symmetry, are classified into lattice types. Considering translations only (no complex occupations of the unit cell with atoms), this gives the minimal set of essentially different lattice types, the *Bravais lattices.* In three dimensions there are 14 Bravais lattices: the seven lattices cubic, trigonal, rhombic, hexagonal, monoclinic, triclinic and tetragonal, defined by the length of and angles between the basis vectors, and variations of these lattices by occupying unit cell faces or the unit cell center with atoms. The according translational operators of a lattice form the *Translation group.*

The rotations of a system (i.e. the according operators) that bring the crystal into itself build the *Rotation group.* There are also *non-symmorphic* symmetries which bring the crystal into itself only with an additional translation (which is not part of the translational group). The according symmetry operations are screw axis and glide planes. In this case these rotations extend the rotation group to the *Point group.* (For symmorphic lattices both are identical.) There are thirty-two different point groups.

The *Space group* consists of the totality of transformations that bring the crystal into itself, containing the translational and the point group as subgroups. There are 230 possible space groups; 157 of them are non-symmorphic, 73 are simple.

Translational symmetry: The translational operator

$$\mathcal{T}_{\mathbf{R}}:\ \mathbf{r} \to \mathbf{r} + \mathbf{R} \tag{2.29}$$

for a lattice vector R commutes with the Hamiltonian. So both operators share a set of eigenvalues. The consequence is the so-called *Bloch theorem*, that states that the wavefunctions can take the form

$$\psi_n(\mathbf{k}, \mathbf{r}) = \varphi_n(\mathbf{k}, \mathbf{r}) e^{i\mathbf{kr}}, \tag{2.30}$$

defining $\mathbf{k}$ (often called the crystal momentum) as a new good quantum number. This vector $\mathbf{k}$ is taken from the reciprocal space, but one can reduce considerations to the first Brillouin zone. The spectrum of energy eigenvalues is periodic in reciprocal space,

$$E(\mathbf{k}) = E(\mathbf{k} + \mathbf{G}), \tag{2.31}$$

$\mathbf{G}$ being a reciprocal lattice vector.

Rotational symmetry: To a rotation in real space, the according symmetry operation in the reciprocal space is the inverse rotation. Analogously to the translations, this reduces the effective reciprocal space you have to consider, leaving as unique part the irreducible wedge of the first Brillouin zone (IBZ).

Consequences for the actual computation are remarked in chapter 4.

2.6 Spin-Density Functional Theory

The spin property of electrons, so far only accounted by a degeneracy factor of two, can be easily incorporated into the theory. It has been shown that the basic Hohenberg-Kohn theorem stands for spin-polarized densities as well. You redefine (in the non-relativistic case) the wavefunctions as spinors

$$\psi_i(\mathbf{r}) = \begin{pmatrix} \psi_{i\uparrow}(\mathbf{r}) \\ \psi_{i\downarrow}(\mathbf{r}) \end{pmatrix}. \tag{2.32}$$

With this slightly different notation, apart from the charge density there arises a second central quantity out of these wavefunctions, the magnetization density $\mathbf{m}(\mathbf{r})$:

$$n(\mathbf{r}) = \sum_{i=1}^{N} \psi_i(\mathbf{r})^* \psi_i(\mathbf{r}) \tag{2.33}$$

$$\mathbf{m}(\mathbf{r}) = \sum_{i=1}^{N} \psi_i(\mathbf{r})^* \sigma \psi_i(\mathbf{r}). \tag{2.34}$$

σ is the vector $(\sigma_x, \sigma_y, \sigma_z)$ of Pauli matrices. The energy is now a functional of these two densities:

$$E = E[n(\mathbf{r}), \mathbf{m}(\mathbf{r})] \tag{2.35}$$

The two spins couple through an effective magnetic field appearing in the modified Kohn-Sham equations. To incorporate the interaction of an external magnetic field $\mathbf{B}_{ext}$ with this spin-polarized system, we include the energy contribution $\mathbf{m}(\mathbf{r}) \cdot \mathbf{B}_{ext}(\mathbf{r})$ into the Kohn-Sham equations and yield

$$\mathcal{H}_1 \psi_i(\mathbf{r}) = \left\{ -\frac{\hbar}{2m} \nabla^2 + V_{eff}(\mathbf{r}) + \sigma \mathbf{B}_{eff}(\mathbf{r}) \right\} \psi_i(\mathbf{r}) = \epsilon_i \psi_i(\mathbf{r}), \tag{2.36}$$

$$\mathbf{B}_{eff}(\mathbf{r}) = \mathbf{B}_{xc}(\mathbf{r}) + \mathbf{B}_{ext}(\mathbf{r}), \tag{2.37}$$

$$\mathbf{B}_{xc}(\mathbf{r}) = \frac{\delta E[n(\mathbf{r}), \mathbf{m}(\mathbf{r})]}{\delta \mathbf{m}(\mathbf{r})}. \tag{2.38}$$

The approximations in section 2.4 can be easily extended for the case of spin-polarized systems.

2.7 Determination of the Total Energy

When the total energy needs to be calculated, the ion-ion interaction E_{ii} of the nuclei

$$E_{ii} = e^2 \sum_{I \neq J} \frac{Z_I Z_J}{|\tau_I - \tau_J|} \tag{2.39}$$

has to be included into the functional (2.11),

$$E_{tot}[n] = T_s[n] + E_H[n] + E_{xc}[n] + E_{ext} + E_{ii}. \tag{2.40}$$

Because of numerical reasons, it is not desirable to calculate the kinetic energy in the form (2.16), applying the double spatial derivative. Instead, one utilizes the Kohn-Sham equations (2.18). Rearranging, multiplying the Bra from the left and summing over all occupied states gives

$$\begin{aligned} -\frac{\hbar}{2m}\nabla^2\psi_i(\mathbf{r}) &= (\epsilon_i - V_{eff}(\mathbf{r}))\,\psi_i(\mathbf{r}), && (2.41)\\ T_s[n] &= -2\sum_{i=1}^{N}\int d^3r\ \psi_i^*(\mathbf{r})\frac{\hbar}{2m}\nabla^2\psi_i(\mathbf{r}) && (2.42)\\ &= \sum_{i=1}^{N}\epsilon_i - \int d^3r\ n(\mathbf{r})V_{eff}(\mathbf{r}) && (2.43) \end{aligned}$$

Putting all the contributions together we obtain

$$\begin{aligned} E[n,\mathbf{m}] &= \sum_{i=1}^{N}\epsilon_i - \int d^3r\ n(\mathbf{r})V_{eff}(\mathbf{r}) && (2.44)\\ &- \int d^3r\ \mathbf{m}(\mathbf{r})\cdot\mathbf{B}_{eff}(\mathbf{r}) && (2.45)\\ &- 4\pi e^2\sum_{I=1}^{M}\int d^3r\ \frac{n(\mathbf{r})Z_I}{|\mathbf{r}-\tau_I|} && (2.46)\\ &- \int d^3r\ n(\mathbf{r})\tilde{V}_{ext}(\mathbf{r}) && (2.47)\\ &+ 4\pi e^2\cdot\frac{1}{2}\int d^3r d^3r'\ \frac{n(\mathbf{r})n(\mathbf{r}')}{|\mathbf{r}-\mathbf{r}'|} && (2.48)\\ &+ \int d^3r\ n(\mathbf{r})\epsilon_{xc}(n(\mathbf{r}),|\mathbf{m}(\mathbf{r})|) && (2.49)\\ &+ 4\pi e^2\sum_{I\neq J}^{M}\frac{Z_I Z_J}{|\tau_I-\tau_J|}, && (2.50) \end{aligned}$$

with the potential $\tilde{V}_{ext}(\mathbf{r})$ due to an electric field external to the system.

2.8 Improvements to Density Functional Theory

Many extensions has been made to the density functional theory, and it is still a subject of continuous development. As we have seen, the observance of spin and the inclusion of external electric and magnetic fields are a natural extension of the theory.

New exchange-correlation functionals are being developed. Methods like the simple scissors operator or the more sophisticated LDA+U theory focus on one of the central drawbacks of the local density (LDA) or generalized gradient approximation (GGA), the mismatching band-gap. The time-dependent density functional theory refines the knowledge about the development of the system in time, and results in a better description of excited states.

The density function theory has proven to be a very powerful tool to treat a many-body problem efficiently and precisely in the framework of a one-particle picture. It has been applied also in a diversity of other disciplines, like superconductivity or astrophysics.

Chapter 3

Dielectric Properties of Solids

Before going into the details of the dielectric function, let us first discuss general properties of physical tensors (of rank two).

3.1 Physical Tensors

Let us connect connect two physical vector quantities linearly via

$$\mathbf{B} = T\mathbf{a}. \tag{3.1}$$

If $\mathbf{B}$ is simply proportional to $\mathbf{a}$ (i.e. pointing in the same direction) T is a scalar factor. But in the general case, T is a tensor of second rank. By its definition, a tensor transforms under a basis change $\mathcal{A}$ to

$$T' = \mathcal{A}T\mathcal{A}^T, \quad \text{or} \quad T'_{ij} = \mathcal{A}_{ik}\mathcal{A}_{jl}T_{kl}. \tag{3.2}$$

Any second-rank tensor can be split up into a symmetric and an antisymmetric part,

$$T_{ij} = \frac{1}{2}(T_{ij} + T_{ji}) + \frac{1}{2}(T_{ij} - T_{ji}), \tag{3.3}$$

but most physical second-rank tensors are purely symmetrical (i.e. $T_{ij} = T_{ji}$), for example the dielectric tensor being subject of this thesis. (One of the few exceptions is the thermoelectric tensor.) Nye [Nye57] remarks that this symmetry property of tensors is not an obvious one, and that the proof necessararily involves thermodynamical considerations.

The behaviour of a symmetric second-rank tensor T_{ij} under coordinate transformation is the same as for the equation

$$T_{ij}x_i x_j = 1, \tag{3.4}$$

which defines a sphere that is either an ellipsoid, a hyperboloid of one or a hyperboloid of two sheets. This equation is called the *representation quadric* for the tensor T_{ij}. An important property of a quadric is the possession of *principal axes*. These are three directions at right angles such that the general quadric (3.4) takes the form

$$T_{11}x_1^2 + T_{22}x_2^2 + T_{33}x_3^2 = 1, \tag{3.5}$$

when referred to these axes.

In a symmetrical tensor referred to arbitrary axes the number of independent components is six. How many independent coefficients remain when referring to its principal axes depends on the symmetry of the crystal in consideration. The *Neumann principle* states that the symmetry elements of any physical property of a crystal must include the symmetry elements of the point group of the crystal. As a result of these considerations, one groups the tensors (or the crystals, accordingly) in the following three so-called *optical classifications*:

Isotropic (Anaxial) crystals: Crystals in which you can choose arbitrarily three crystallographically equivalent orthogonal axes. These three axes are the principal axes of the tensor. All diagonal elements are equal (see table below), and the crystall acts like an amorphous medium.

Uniaxial tensors: Crystals without three orthogonal equivalent axes, but with two or more these axes in one plane. This is the case for the tricline, trigonal and hexagonal lattices. The plane with the equivalent axes is perpendicular to the three-fold, four-fold or six-fold symmetry axis, respectively. One of the optical axes coincides with this symmetry axes, the others form a pair of orthogonal axes in the plane.

Biaxial tensors: Crystals with lower symmetry. For orthorombic crystals, the tensor possesses diagonal form with each different elements. The optical axes coincide with the crystal axes. In monocline and tricline systems, the optical axes are not alleged. (In this case, it would be possible to rotate the axes of the tensor such that only the three principal coefficients are necessary, but one would have no information regarding the orientation of the representation's sphere relative to the crystallographic axes [Lov89].)

The corresponding shape of the tensors is taken from a table of ([Nye57]).

In most cases of calculations the used basis vectors coincide with the optical axes of the crystal in study.

3.2 Macroscopic Optics

We make a macroscopic approach to the electromagnetic description of a matter. Its properties a described by the

Classification	Crystal System	Indep. Coeff.	Tensor shape
Anaxial	Cubic	1	$\begin{pmatrix} T & 0 & 0 \\ 0 & T & 0 \\ 0 & 0 & T \end{pmatrix}$
Uniaxial	Tetragonal Hexagonal Trigonal	2	$\begin{pmatrix} T_1 & 0 & 0 \\ 0 & T_1 & 0 \\ 0 & 0 & T_3 \end{pmatrix}$
Biaxial	Orthorhombic	3	$\begin{pmatrix} T_1 & 0 & 0 \\ 0 & T_2 & 0 \\ 0 & 0 & T_3 \end{pmatrix}$
	Monoclinic	4	$\begin{pmatrix} T_{11} & 0 & T_{31} \\ 0 & T_2 & 0 \\ T_{31} & 0 & T_{33} \end{pmatrix}$
	Triclinic	6	$\begin{pmatrix} T_{11} & T_{12} & T_{31} \\ T_{12} & T_{22} & T_{23} \\ T_{31} & T_{23} & T_{33} \end{pmatrix}$

Table 3.1: Shapes of second-rank tensors for different crystal structures.

Maxwell equations:

$$\begin{aligned}
\nabla \times \mathbf{E}(\mathbf{r},t) &= -\frac{\partial}{\partial t}\mathbf{B}(\mathbf{r},t) && (3.6)\\
\nabla \cdot \mathbf{D}(\mathbf{r},t) &= \rho(\mathbf{r},t) && (3.7)\\
\nabla \times \mathbf{H}(\mathbf{r},t) &= \mathbf{j}(\mathbf{r},t) + \frac{\partial}{\partial t}\mathbf{D}(\mathbf{r},t) && (3.8)\\
\nabla \cdot \mathbf{B}(\mathbf{r},t) &= 0, && (3.9)
\end{aligned}$$

with **E**, **D** the electric field and the electric displacement, **B** the magnetic induction and **H** the magnetic field. ρ and **j** describe the external charges and currents. The induces ones vanish by the averaging done for this macroscopic approach. This description is complete only if the coupling between the **D** and **E**, and between **B** and **H**, respectively, is given.

Material coefficients: To describe the response linearly, one introduces two coupling functions (also called constants frequently), the dielectric function ε (also known as permittivity) and the magnetic permeability μ:

$$\mathbf{D} = \varepsilon\varepsilon_0\mathbf{E}, \quad \mathbf{B} = \mu\mu_0\mathbf{H}, \tag{3.10}$$

or alternatively defining the electric polarizability **P** and the magnetization **M** by

$$\mathbf{D} = \varepsilon_0\mathbf{E} + \mathbf{P},\ \mathbf{P} = \alpha_p\mathbf{E} = \chi\varepsilon_0\mathbf{E}, \tag{3.11}$$

$$\mathbf{H} = \frac{1}{\mu_0}\mathbf{B} - \mathbf{M},\ \mathbf{M} = \frac{1}{\chi_m\mu_0}\mathbf{H}, \tag{3.12}$$

defining the electric and magnetic susceptibilities χ and χ_m and the polarizability α_p as

$$\varepsilon = 1 + \chi, \quad \alpha_p = \varepsilon_0\chi, \tag{3.13}$$

$$\mu = 1 - \chi_m, \quad \chi \tag{3.14}$$

The magnetic susceptibility is not given attention anymore. When coupling the current **j** linearly to the electric field according to Ohm's law, you introduce the electrical conductivity σ:

$$\mathbf{j} = \tilde{\sigma}\mathbf{E}. \tag{3.15}$$

Absorption of waves: In vacuum, the electric field of a free electro-magnetic wave follows the wave equation

$$\triangle\mathbf{E}(\mathbf{r},t) = \mu_0\varepsilon_0\varepsilon\frac{\partial^2}{\partial t^2}\mathbf{E}(\mathbf{r},t), \tag{3.16}$$

which has solutions

$$\mathbf{E}(\mathbf{r},t) = \mathbf{E}_0 e^{i(\mathbf{kr}-\omega t)}. \tag{3.17}$$

When penetrating matter, the amplitude lowers exponentially,

$$E = E_0 e^{-}, \tag{3.18}$$

with the absorption coefficient α defined as

$$\frac{dI}{dz} = -\alpha I \tag{3.19}$$

for penetration in z-direction, and $I = |E|^2$ the amplitude.

The rest...

Elementary classics (see Madelung [Mad78]): We assume a classical electromagnetic wave of form

$$\vec{A}(\vec{r},t) = \vec{A}_0 e^{i(\vec{K}\vec{r}-\omega t)} = A_0 \vec{e} e^{i(\frac{\tilde{n}}{c}\vec{\omega}\vec{r}-\omega t)}$$

with complex refractive index $\tilde{n}(\omega) = n(\omega) + i\kappa(\omega)$. If refraction and dielectricity are coupled by $\epsilon(\omega) = \tilde{n}^2(\omega)$ with $\epsilon(\omega) = \epsilon_1(\omega) + i\epsilon_2(\omega)$ complex, we get the connection

$$\begin{aligned} n^2 - \kappa^2 &= \epsilon_1 \qquad (3.20) \\ 2n\kappa &= \epsilon_2. \qquad (3.21) \end{aligned}$$

Another well mesurable quantity is the relexion of a perpendicular incoming wave $R(\omega)$ which is related to $n(\omega)$ and $k(\omega)$ by

$$R = \left(\frac{1-\tilde{n}}{1+\tilde{n}}\right) = \frac{(n-1)^2 + k^2}{(n+1)^2 + k^2}.$$

Tensor properties: In the general case, the coupling (3.10) is not simple scalar, but tensor-like, as well as depending on the frequency and the location. Since the coupling is homogeneous in time, and for the macroscopic approach also in space, the arguments of the susceptibilities read (with the array boundaries making the statements causal, or an appropiate defined susceptiblilty)

$$\begin{aligned} \mathbf{P}(\mathbf{r},t) &= \int d^3r' \int dt' \; \tilde{\chi}(\mathbf{r}-\mathbf{r}', t-t')\mathbf{E}(\mathbf{r}',t') \qquad (3.22) \\ \mathbf{M}(\mathbf{r},t) &= \int d^3r' \int dt' \; \tilde{\chi}_m(\mathbf{r}-\mathbf{r}', t-t')\mathbf{H}(\mathbf{r}',t') \qquad (3.23) \end{aligned}$$

In Fourier space this convolution gives

$$\begin{aligned} \mathbf{P}(\mathbf{k},\omega) &= \tilde{\chi}(\mathbf{k},\omega)\mathbf{E}(\mathbf{k},\omega) \qquad (3.24) \\ \mathbf{M}(\mathbf{k},\omega) &= \tilde{\chi}_m(\mathbf{k},\omega)\mathbf{H}(\mathbf{k},\omega). \qquad (3.25) \end{aligned}$$

Headwords:

- relectivity, transmitivity, extinction
- Beer's law, scattering cross section
- refractive index, (complex) dielectric function
- eps1 - refraction, eps2 - absorption
- Reflection R=r(n,kappa)
- Kramers-Kronig

For finite temperatures, system is not describable by a wave function. statistical averaging needed. (springer,S250)

XXX RPA?

- kramers-kronig relations
- Transformations.

3.3 Relation between real and imaginary part

Background: Due to the Dirac relation

$$\frac{1}{\omega + i\epsilon} = \mathcal{P}\frac{1}{\omega} + i\pi\delta(\epsilon) \tag{3.26}$$

a spectral distribution function with an energylike parameter ω

$$G(\omega) = \lim_{\varepsilon\to 0}\frac{1}{N}\int d^3k \frac{F(\mathbf{k})}{E - E(\mathbf{k}) - i\varepsilon} \tag{3.27}$$

has its real and imaginary parts

$$\Re G(\omega) = \mathcal{P}\frac{1}{N}\int d^3k \ \frac{F(\mathbf{k})}{\omega - \omega(\mathbf{k})} \tag{3.28}$$

and

$$\Im G(\omega) = \frac{\pi}{N}\int d^3k \ F(\mathbf{k})\delta(\omega - \omega(\mathbf{k})), \tag{3.29}$$

which are the Hilbert transforms of each other.

Consequence: Kramers-Kronig Relation These relations connect the real and imaginary part of any parameter that relates two fields in a linear and causal way. The relations read

$$\begin{aligned} \epsilon_1(\omega) &= 1+ \tfrac{1}{\pi}\mathcal{P}\int\limits_{-\infty}^{+\infty} d\eta \tfrac{\epsilon_2(\eta)}{\eta-\omega} \\ \epsilon_2(\omega) &= - \tfrac{1}{\pi}\mathcal{P}\int\limits_{-\infty}^{+\infty} d\eta \tfrac{\epsilon_1(\eta)-1}{\eta-\omega}. \end{aligned} \tag{3.30}$$

$\mathcal{P}$ denotes the principal value of the integral. Since $\omega > 0$ it is desirable to transform (3.32) to integrals over the domain (0∞). We use the relation

$$\varepsilon(-\omega) = \varepsilon_1(-\omega) + \frac{i\sigma(-\omega)}{-\omega} = \varepsilon^*(\omega) \tag{3.31}$$

By multiplying both the numerator and demoninator of (3.30) with $(\eta+\omega)$, one yields

$$\begin{aligned} \epsilon_1(\omega) &= 1+ \tfrac{2}{\pi}\mathcal{P}\int\limits_{0}^{\infty} d\eta \tfrac{\omega'\epsilon_2(\eta)}{\eta^2-\omega^2} \\ \epsilon_2(\omega) &= - \tfrac{2}{\pi}\mathcal{P}\int\limits_{0}^{\infty} d\eta \tfrac{\epsilon_1(\eta)-1}{\eta^2-\omega^2}. \end{aligned} \tag{3.32}$$

The consequence of the Kramers-Kronig relations is that once the imaginary part is known for the whole spectrum, you know the real part as well, and vice versa. It is also worth to notice that these relations are of universal validity since they do not imply any knowledge of the interactions inside the solid.

One can also construct Kramers-Kronig relations for other quantities, like the magnitude and the phase of the complex reflection coefficient.

3.4 Ideas

Effective mass
oszillator strength
conductivity...

3.5 Transmission spectra

- bandgap - absorption edge
- photonic range
- electronic/interband absorption
- anisotropy
- cubic same in all directions

3.6 Classical Models

- classical, semi-classical, fully quantum mechanical model
- oszillator model
- Lorentz (Tauc-Lorentz?)
- gas: ω_C, plasma frequency

3.7 Dielectric function

Microscopic means local, macroscopic means averaged.

Here relation to one-particle image. Missing many-particle effects, excitations)

3.7.1 Microscopic definition, dielectricity

Microscopic Maxwell equations are

$$\begin{aligned}&\nabla\cdot\mathbf{e}=\frac{\rho_{mic}}{\varepsilon_0},\quad \nabla\times\mathbf{b}=\mu_0\mathbf{j_{mic}}+\mu_0\varepsilon_0\frac{\partial}{\partial t}\mathbf{e}\\&\nabla\cdot\mathbf{b}=0,\quad \nabla\times\mathbf{e}=-\frac{\partial}{\partial t}\mathbf{b}\end{aligned}$$

with $\mathbf{e}=\mathbf{e}(\mathbf{r},t)$ the microscopic electric field and $\mathbf{b}=\mathbf{b}(\mathbf{r},t)$ the microscopic magnetic induction. You acquire the macroscopic quantities by averaging:

$$\rho=\langle\rho_{mic}\rangle,\quad \mathbf{j}=\langle\mathbf{j}_{mic}\rangle,\quad \mathbf{E}=\langle\mathbf{e}\rangle,\quad \mathbf{B}=\langle\mathbf{b}\rangle. \tag{3.33}$$

Now additionally ....

$$\mathbf{D}=\varepsilon_0\mathbf{E}+\mathbf{P},\quad \mathbf{H}=\frac{1}{\mu_0}\mathbf{B}-\mathbf{M} \tag{3.34}$$

Definition of dielectric function and inverse:

$$\begin{aligned}\mathbf{E}(\mathbf{r},t)&=\varepsilon_0^{-1}\int d^3r'\int dt'\varepsilon_{mac}^{-1}(\mathbf{r}-\mathbf{r}',t-t')\mathbf{D}(\mathbf{r}',t')\\\mathbf{e}(\mathbf{r},t)&=\varepsilon_0^{-1}\int d^3r'\int dt'\varepsilon_{mic}^{-1}(\mathbf{r},\mathbf{r}',t-t')\mathbf{D}(\mathbf{r}',t')\end{aligned}$$

where ε is a tensor. Medium is homogenous from macroscopic point of view, but not microscopic; there only lattice periodicity. DF and inverse obey the relation

$$\varepsilon_{mic}^{-1}(\mathbf{r},\mathbf{r}',t-t')\varepsilon_{mic}(\mathbf{r}',\mathbf{r}'',t'-t'')=\delta(\mathbf{r}-\mathbf{r}')\delta(\mathbf{r}'-\mathbf{r}'')\delta(t-t')\delta(t'-t'') \tag{3.35}$$

3.7.2 Fourier transforms

Now fourier transforms [1] of the macroscopic electric field:

$$\mathbf{E}(\mathbf{q},\omega) = \varepsilon_0^{-1}\varepsilon_{mac}^{-1}(\mathbf{q},\omega)\mathbf{D}(\mathbf{q},t) \tag{3.36}$$

The microscopic one:

$$\begin{aligned}\varepsilon_{mic}(\mathbf{r}+\mathbf{R},\mathbf{r}'+\mathbf{R},t-t') &= \varepsilon_{mic}(\mathbf{r},\mathbf{r}',t-t')\\ \Rightarrow \varepsilon_{mic}(\mathbf{q},\mathbf{q}',\omega) &= e^{i(\mathbf{q}iqR-\mathbf{q}')\mathbf{R}}\varepsilon_{mic}(\mathbf{q},\mathbf{q}',\omega)\end{aligned}$$

with R a reciprocal lattice vector. Since this means ε is only non-zero for a difference $\mathbf{q}-\mathbf{q}'$ equal to a reciprocal lattice vector, we make the following change in notation:

$$\varepsilon_{mic}(\mathbf{q},\mathbf{q}',\omega) \to \varepsilon_{mic}(\mathbf{k}+\mathbf{G},\mathbf{k}+\mathbf{G}',\omega), \tag{3.37}$$

which means

$$\begin{gathered}\int d^3q \to \int_{BZ} d^3k \sum_{\mathbf{G}},\\ \int d^3q \int d^3q' \to \int_{BZ} d^3k \sum_{\mathbf{G},\mathbf{G}'},\\ \varepsilon^{-1}(\mathbf{k}+\mathbf{G},\mathbf{k}+\mathbf{G}')\varepsilon(\mathbf{k}+\mathbf{G}',\mathbf{k}+\mathbf{G}'') = \delta_{\mathbf{G}\mathbf{G}'}\delta_{\mathbf{G}'\mathbf{G}''}\end{gathered}$$

Together with the definition (3.33) this results in the following fourier transform for the microscopic dielectric function:

$$\begin{aligned} & \sum_{\mathbf{G}}\int d^3k \int d\omega\ e^{i((\mathbf{k}+\mathbf{G})r-\omega t)}\mathbf{e}(\mathbf{k}+\mathbf{G},\omega)\\ = & \int d^3r' \left(\sum_{\mathbf{G},\mathbf{G}'}\int d^3k \int d\omega\ e^{i((\mathbf{k}+\mathbf{G})\mathbf{r}+(\mathbf{k}+\mathbf{G}')\mathbf{r}'-\omega t)}\varepsilon_{mic}(\mathbf{q},\mathbf{q}',\omega)\right)\cdot\\ & \left(\sum_{\mathbf{G}''}\int d^3k'' \int \omega'' e^{i((\mathbf{k}''+\mathbf{G}'')\mathbf{r}-\omega'' t)}\mathbf{D}(\mathbf{q}'',\omega'')\right)\\ \Rightarrow & \ \mathbf{e}(\mathbf{k}+\mathbf{G},\omega)\\ = & \sum_{\mathbf{G}'}\varepsilon(\mathbf{k}+\mathbf{G},\mathbf{k}+\mathbf{G}')\sum_{\mathbf{G}''}\int d^3k''\mathbf{D}(\mathbf{k}''+\mathbf{G}'')\int d^3r' e^{i(\mathbf{k}+\mathbf{G}'+\mathbf{k}''+\mathbf{G}'')}\\ = & \sum_{\mathbf{G}'}\varepsilon(\mathbf{k}+\mathbf{G},\mathbf{k}+\mathbf{G}')\sum_{\mathbf{G}''}\int d^3k''\mathbf{D}(\mathbf{k}''+\mathbf{G}'')\delta(\mathbf{k}+\mathbf{G}'+\mathbf{k}''+\mathbf{G}'')\\ = & \sum_{\mathbf{G}'}\varepsilon(\mathbf{k}+\mathbf{G},\mathbf{k}+\mathbf{G}')\mathbf{D}(\mathbf{k}+\mathbf{G}')\end{aligned}$$

---

[1] In the following the Fourier transforms are written in the form $f(\mathbf{r},t) = \frac{1}{2\pi}\int d^3\mathbf{q}\int d\omega\ \exp(i(\mathbf{qr}-\omega t))f(\mathbf{q},\omega)$ and $f(\mathbf{q},\omega) = \int d^3\mathbf{r}\int dt\ \exp(-i(\mathbf{qr}-\omega t))f(\mathbf{r},t)$, so the kind of function is identifiable by its parameters. Also only partly fourier transformed functions may appear.

3.7.3 dielectricity ↔ internal charge density

Next: Averaging...(244-246) With the fourier transforms of two maxwell equations

$$\imath \mathbf{q}\mathbf{e}(\mathbf{q}) = \frac{1}{\varepsilon_0}\rho^{mic}(\mathbf{q}), \quad \imath \mathbf{q}\mathbf{D}(\mathbf{q}) = \rho^{ext}(\mathbf{q}), \tag{3.38}$$

we conclude to

$$\begin{aligned} \rho^{ext}(\mathbf{k}+\mathbf{G}) &= \sum_{\mathbf{G}'}(\mathbf{k}+\mathbf{G})\varepsilon(\mathbf{k}+\mathbf{G},\mathbf{k}+\mathbf{G}')\frac{\rho^{mic}(\mathbf{k}+\mathbf{G}')(\mathbf{k}+\mathbf{G}')}{(\mathbf{k}+\mathbf{G}')^2} \\ & \sum_{\mathbf{G}'}|\mathbf{k}+\mathbf{G}|\ |\mathbf{k}+\mathbf{G}'|\ \varepsilon(\mathbf{k}+\mathbf{G},\mathbf{k}+\mathbf{G}')\frac{\rho^{ext}(\mathbf{k}+\mathbf{G})+\rho^{ind}_{mic}(\mathbf{k}+\mathbf{G}')}{(\mathbf{k}+\mathbf{G}')^2} \end{aligned}$$

with $\varepsilon(\mathbf{k}+\mathbf{G},\mathbf{k}+\mathbf{G}') = u_{\mathbf{k}+\mathbf{G}}\varepsilon(\mathbf{k}+\mathbf{G},\mathbf{k}+\mathbf{G}')u_{\mathbf{k}+\mathbf{G}'}$ the longitudinal dielectric function ($u_{\mathbf{k}} = \frac{\mathbf{k}}{|\mathbf{k}|}$ unit vector).

Using the fourier transform $\rho^{ext}(\mathbf{q}) = \varepsilon_0 \cdot \mathbf{q}^2 U^{ext}(\mathbf{q})$, we transform to

$$\begin{aligned} &\sum_{\mathbf{G}}\varepsilon^{-1}(\mathbf{k}+\mathbf{G}'',\mathbf{k}+\mathbf{G})\varepsilon_0\cdot(\mathbf{k}+\mathbf{G})^2U^{ext}(\mathbf{k}+\mathbf{G}) = \\ &\quad \sum_{\mathbf{G},\mathbf{G}'}|\mathbf{k}+\mathbf{G}|\ |\mathbf{k}+\mathbf{G}'|\ \varepsilon^{-1}(\mathbf{k}+\mathbf{G}'',\mathbf{k}+\mathbf{G})\varepsilon(\mathbf{k}+\mathbf{G},\mathbf{k}+\mathbf{G}')\left(\varepsilon_0U^{ext}(\mathbf{k}+\mathbf{G}')+\frac{\rho^{ind}_{mic}(\mathbf{k}+\mathbf{G})}{(\mathbf{k}+\mathbf{G}')^2}\right), \end{aligned}$$

which results in

$$\rho^{ind}_{mic}(\mathbf{k}+\mathbf{G}) = \varepsilon_0\sum_{\mathbf{G}'}\left(\varepsilon^{-1}(\mathbf{k}+\mathbf{G},\mathbf{k}+\mathbf{G}')-\delta_{\mathbf{G}\mathbf{G}'}\right)|\mathbf{k}+\mathbf{G}|\ |\mathbf{k}+\mathbf{G}'|U^{ext}(\mathbf{k}+\mathbf{G}')$$

and

$$\varepsilon^{-1}(\mathbf{k}+\mathbf{G},\mathbf{k}+\mathbf{G}') = \delta_{\mathbf{G}\mathbf{G}'} + \tfrac{\varepsilon^{-1}}{|\mathbf{k}+\mathbf{G}|\ |\mathbf{k}+\mathbf{G}'|}\tfrac{\partial\rho^{ind}_{mic}(\mathbf{k}+\mathbf{G})}{\partial U^{ext}(\mathbf{k}+\mathbf{G})}$$

3.8 Quantum mechanical model

- Indirect transitions:
- Direct Transitions...

3.9 Comparison

Possible reasons

- DFT doesn't describe excited states
- just quasi-particles
- other contributions: xxx

3.10 Missing

Missing:

- local field corrections (Fox, 2.2.3)
- RPA

$$\varepsilon_2^{\alpha\beta} = \frac{4\pi^2 e^2}{m^2\omega^2} \sum_{i,j} \int\limits_{\hbar\omega = E_j(\vec{k}) - E_i(\vec{k})} \frac{dk^2}{(2\pi)^3} \frac{\langle i\vec{k}|p_\alpha|j\vec{k}\rangle\langle i\vec{k}|p_\alpha|j\vec{k}\rangle}{\left|\nabla_{\vec{k}}\left(E_j(\vec{k}) - E_i(\vec{k})\right)\right|} f_0(E_i(\vec{k}))(1 - f_0(E_j(\vec{k}))) \tag{3.39}$$

$$\varepsilon_2 = \sum_{\alpha,\beta} \varepsilon_2^{\alpha\beta} e_\alpha e_\beta, \tag{3.40}$$

For the cubic case:

$$\varepsilon_2 = \frac{4\pi^2 e^2}{m^2\omega^2} \sum_{i,j} \int\limits_{\hbar\omega = E_j(\vec{k}) - E_i(\vec{k})} \frac{dk^2}{(2\pi)^3} \frac{|\langle i\vec{k}|p|j\vec{k}\rangle|^2}{\left|\nabla_{\vec{k}}\left(E_j(\vec{k}) - E_i(\vec{k})\right)\right|} f_0(E_i(\vec{k}))(1 - f_0(E_j(\vec{k}))) \tag{3.41}$$

What about prefactor? Atomic units, $\rightarrow \cdot \frac{4\pi}{\varepsilon_0}$.
Definition of JDOS:

$$J(E) = \sum_{i,j} \int\limits_{E = E_j(\vec{k}) - E_i(\vec{k})} \frac{dk^2}{(2\pi)^3} \frac{1}{\left|\nabla_{\vec{k}}\left(E_j(\vec{k}) - E_i(\vec{k})\right)\right|} \tag{3.42}$$

3.11 Krasovskii

$\varepsilon = \varepsilon_{intra} + \varepsilon_{inter}$
$\varepsilon_{1intra} = 1 - \frac{\omega_p^2}{\omega^2}$
$\varepsilon_{2intra} \sim \omega_p^2 \frac{\partial}{\partial\omega}\delta(\omega)$

$$\langle \imath\mathbf{k}|\nabla|\imath\mathbf{k}\rangle = \frac{1}{\hbar}\frac{\partial E_\imath(\mathbf{k})}{\partial\mathbf{k}} \tag{3.43}$$

Types of critical points? (e.g. Dragoman p.9)

Chapter 4

Basis sets

As already mentioned in section 2.3, the eigenfunctions are usually expanded in a basis,

$$\langle \mathbf{r}|i\mathbf{k}\rangle = \psi_i(\mathbf{k},\mathbf{r}) = \frac{1}{\sqrt{\Omega}}\sum_{\mathbf{G}} C^i_{\mathbf{k}+\mathbf{G}}\phi_{\mathbf{k}+\mathbf{G}}(\mathbf{r}), \tag{4.1}$$

where Ω is the unit cell volume. The Hamilton and overlap matrices $\mathcal{H}$ and $\mathcal{S}$ are constructed for a set of k-points, and the generalized eigenvalue problem

$$\left[\mathcal{H}(\mathbf{k}) - \epsilon_i\mathcal{S}(\mathbf{k})\right]\mathbf{c}_i(\mathbf{k}) = 0 \tag{4.2}$$

is solved, with $\mathbf{c}_i(\mathbf{k}) = (C^i_{\mathbf{k}+\mathbf{G}})$ the vector of the C-coefficients (of eigenvalue i and vector $\mathbf{k}$) for all $\mathbf{G}$'s. Many questions of detail, as well as general properties of your calculation like accuracy and computational effort depend on the choice of your basis set.

The better the basis functions match the shape of the actual wavefunctions, the better the convergence is. Some basis sets may have drawbacks that can not always be lifted by a bigger cut-off.

4.1 The Plane-Wave Basis

A very simple basis set is build out of plane waves (PWs), the eigenfunctions for a constant potential, that are free electrons

$$\phi_{\mathbf{k}+\mathbf{G}}(\mathbf{r}) = e^{i(\mathbf{k}+\mathbf{G})\mathbf{r}},$$

The use of this basis complies to a simple fourier transform. Typically this is a good choice for nearly free electrons and delocalized electrons.

The simple analytic form usually leads to well-performing calculations that are straight-forward to implement. The hamilton and overlap matrices can easily be calculated as

$$\begin{aligned}
\mathcal{H}_{\mathbf{G},\mathbf{G}'}(\mathbf{k}) &= \frac{\hbar^2}{2m}|\mathbf{k}+\mathbf{G}|^2\delta_{\mathbf{G}\mathbf{G}'} + V_{(\mathbf{G}-\mathbf{G}')}, \\
V_{(\mathbf{G}-\mathbf{G}')} &= \int\limits_{uc} d^3r \; e^{-i(\mathbf{G}-\mathbf{G}')\mathbf{r}} \; V_{eff}(\mathbf{r}) \\
\mathcal{S}_{\mathbf{G},\mathbf{G}'} &= \delta_{\mathbf{G}\mathbf{G}'}
\end{aligned} \tag{4.3}$$

The matrix elements of the momentum operator for instance in this basis (in terms of the *eigen*functions) give

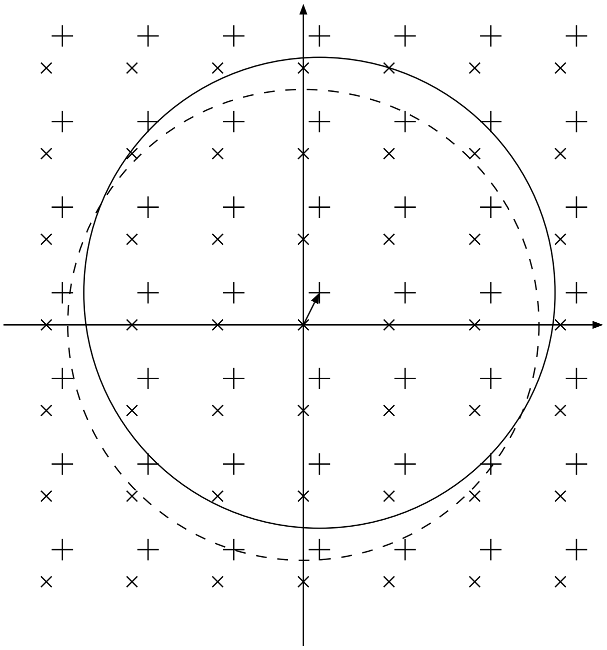

Figure 4.1: Used G-vectors in expansion. Small x-like crosses indicate the basis vectors of reciprocal space. The plus-like crosses indicate the $(\mathbf{k}+\mathbf{G})$-vectors corresponding to the $\mathbf{k}$-vector drawn in the origin. The large circle encloses all vectors of $|\mathbf{G}| < G_{max}$, the smaller one those of $|\mathbf{k}+\mathbf{G}| < G_{max}$.

$$\langle f\mathbf{k}|\tfrac{\nabla}{i}|i\mathbf{k}\rangle_{PW} = \frac{1}{\Omega}\sum_{\mathbf{G}}(\mathbf{k}+\mathbf{G})C^{f*}_{\mathbf{k}+\mathbf{G}}C^{i}_{\mathbf{k}+\mathbf{G}}. \tag{4.4}$$

The choice of $\mathbf{G}$-vectors is illustrated in figure 4.1. After choosing a cut-off value G_{max}, all $(\mathbf{k}+\mathbf{G})$-vectors are used that obey $|\mathbf{k}+\mathbf{G}| \leq G_{max}$. This choice is necessary because of numerical reasons. The number of basis functions obviously depends on the k-point in consideration.

Potentials: XX , and less efficient for systems including localized valence electrons, like transition metals.

The price for this simplicity is the inability of this basis set to describe the strong interactions including the nuclear potential $\sim \frac{1}{r}$. As a solution, the idea of *pseudopotentials* has been developed. The potentials are identical to the all-electron potential outside a given core-radius, but of different, smoother shape inside. They are constructed just that the resulting pseudo-wavefunction mimics the all-eletron wavefunction outside this radius as close as possible. For many elements, this method works reliable, yielding smooth potentials.

4.2 The APW method

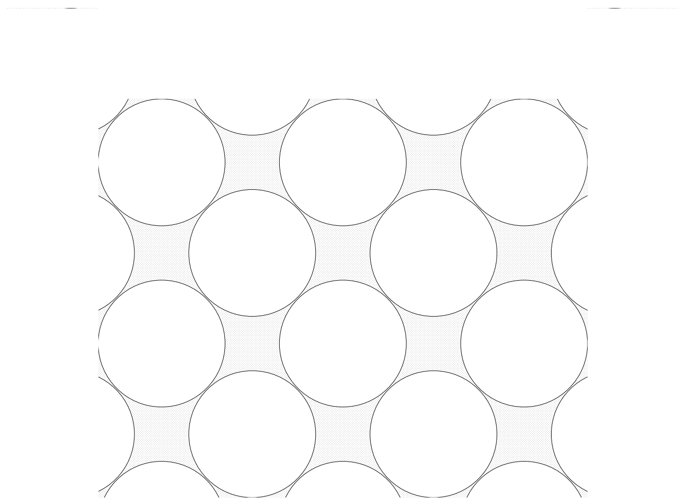

Figure 4.2: Spatial partitioning in augmented basis sets. The circles are the muffin tins, leaving the interstitial region, plotted grayed.

A basis set of better shape has been proposed by Slater already in 1937 [Sla37]. In this *Augmented PlaneWave* (APW) basis, space is divided into spheres that are centered around each atom, so-called muffin-tins (MTs), and into the remaining interstitial region (IS)[1]. While plane waves are used as basis functions

---

[1] For non-bulk systems, different choices can be made. For slabs, an additional vacuum region

in the interstitial, they are augmented in the spheres by spherical harmonics time radial basis functions that are solutions to of the radial Schrödinger equation to an l-dependent energy

$$\left\{-\frac{\hbar^2}{2m}\frac{\partial^2}{\partial r^2}+\frac{\hbar^2}{2m}\frac{l(l+1)}{r^2}+V(r)-E_l\right\} r u_l(r)=0. \tag{4.5}$$

Expanding the function in a series of these functions up to an l-cutoff l_{max}, this gives the basis functions (the augmented plane waves)

$$\phi_{\mathbf{k}+\mathbf{G}}(\mathbf{r})=\begin{cases} e^{i(\mathbf{k}+\mathbf{G})\mathbf{r}} & \mathbf{r}\in \mathrm{IS} \\ \sum\limits_{l=0}^{l_{max}}\sum\limits_{m=-l}^{l} a^{\alpha}_{lm}(\mathbf{k}+\mathbf{G})u_l(r,E_l)Y_{lm}(\hat{\mathbf{r}}) & \mathbf{r}\in \mathrm{MT}_{\alpha}. \end{cases} \tag{4.6}$$

The calculation of matrix elements becomes more complicated due to the radial functions being non-orthogonal when restricted to the muffin-tins, and due to the complex shape of the interstitial region.

It is useful to normalize the radial functions like

$$\langle u_l|u_l\rangle=\int\limits_0^{R_\alpha} dr\ |u_l|^2=1 \tag{4.7}$$

To ensure that these basis functions are continuous, one has to match the muffin-tin functions to the planewaves on the boundaries. To arrange this, one expands the spherical harmonics into planewaves using the Rayleigh relation

$$e^{i\mathbf{K}\mathbf{r}}=4\pi\sum_{lm} i^l j_l(rK)Y^*_{lm}(\hat{\mathbf{K}})Y_{lm}(\hat{\mathbf{r}}). \tag{4.8}$$

$K=|\mathbf{K}|$ is the length of the vector $\mathbf{K}=\mathbf{k}+\mathbf{G}$, and j_l is the Bessel function of the first kind. An atom α at position $\mathbf{S}_\alpha$ owns a coordinate frame $(\mathcal{U}_\alpha,\mathbf{S}_\alpha)$ (in the style of symmetry operations **??**, $\mathcal{U}_\alpha$ being the rotation matrix). In this frame, a plane-wave takes the form

$$e^{i\mathbf{K}\mathbf{r}}\to e^{i(\mathcal{U}_\alpha\mathbf{K})(\mathbf{r}+\mathcal{U}_\alpha\mathbf{S}_\alpha)} \tag{4.9}$$

Matching the planewaves on the sphere boundaries with the muffin-tin functions for every augmented wave gives the a-coefficients as

$$a^{\alpha}_{lm}(\mathbf{K})=e^{i\mathbf{K}\mathbf{S}_\alpha}\frac{4\pi i^l}{u_l(R_\alpha,E_l)}j_l(KR_\alpha)Y^*_{lm}(\mathcal{U}_\alpha\hat{\mathbf{K}}). \tag{4.10}$$

This leaves the C-coefficients (and the energies E_l) as the variational parameters of the method, the a's being determined by them. In fact this matching works

---

is introduced as a two half-spaces, expanding the function in decaying exponentials [Kur00].

only on a few points exactly, but the so-chosen A-coefficients yield the smallest mismatch.

With these basis functions the wavefunction take the form

$$\psi_i(\mathbf{k},\mathbf{r}) = \begin{cases} \frac{1}{\sqrt{\Omega}} \sum_{\mathbf{G}} C^i_{\mathbf{k}+\mathbf{G}} e^{i(\mathbf{k}+\mathbf{G})\mathbf{r}} & \mathbf{r} \in \mathrm{IS} \\ \sum_{\mathbf{G}} \sum_{lm} C^i_{\mathbf{k}+\mathbf{G}} a^{\alpha}_{lm}(\mathbf{k}+\mathbf{G}) u_l(r, E_l) Y_{lm}(\hat{\mathbf{r}}) & \mathbf{r} \in \mathrm{MT}_\alpha \end{cases} \tag{4.11}$$

Since the a-coefficients are – together with the expansion coefficients C – the only terms inside the spheres depending on $\mathbf{G}$, one can write the whole wavefunction shorter as

$$\psi_i(\mathbf{k},\mathbf{r}) = \begin{cases} \frac{1}{\sqrt{\Omega}} C^i_{\mathbf{k}+\mathbf{G}} e^{i(\mathbf{k}+\mathbf{G})\mathbf{r}} & \mathbf{r} \in \mathrm{IS} \\ \sum_{lm} A^{i,\alpha}_{lm}(\mathbf{k}) u_l(r, E_l) Y_{lm}(\hat{\mathbf{r}}) & \mathbf{r} \in \mathrm{MT}_\alpha \end{cases} \tag{4.12}$$

with the shorthand

$$A^{i,\alpha}_{lm}(\mathbf{k}) = \sum_{\mathbf{G}} C^i_{\mathbf{k}+\mathbf{G}} a^{\alpha}_{lm}(\mathbf{k}+\mathbf{G}). \tag{4.13}$$

Potentials: Since these basis functions are the solutions of a constant potential in the interstitial and a spherical potential in the muffin tins, this *muffin-tin approximation* for the shape of the potentials has initially been used. In the *warped* muffin-tin approximation, the interstitial potential is extended to general shape, that means extended in planewaves.

Problems of the method: According to (4.10) the A's are determined completely by the planewave coefficients. So these C coefficients together with the energy parameters E_l are the variational parameters of this method. If the energy parameters were taken as fixed rather than as a variational parameter, the method would simply consist of the use of the APW basis set with solving the secular equation (4.1). The solutions would give the band energies.

Unfortunately, this is not a workable scheme. The basis functions lack variational freedom, this means they do not yield correct results if the energy parameters E_l mismatch the actual band energies. This means that these energies for one k-point can not be obtained from a single diagonalization, but it has to be solved iteratively. This makes this method much more computationally demanding.

Furthermore it is difficult to use a general potential beyond the warped muffin-tin approximation [Sin94]. Another obstacle is the so-called asymptote problem. There might be energy parameters for which u_l vanishes or becomes very small on the sphere boundary. As a consequence the planewaves and the radial functions become decoupled.

4.3 The LAPW method

Much work has been devoted to lifts the described problems. In 1975, Andersen introduced the *Linearized Augmented Plane Wave* (LAPW) method. The central idea is to describe the basis functions inside the muffin-tins not only by solutions of the radial Schrödinger equation $u_l(r, E_l)$, but as well by its energy derivates $\dot{u}_l(r, E_l) \equiv \frac{\partial}{\partial E} u_l(r, E_l)$. If E_l differs slightly from the true band energy ϵ, according to an expansion with respect to the energy,

$$u_l(r, \epsilon) = u_l(r, E_l) + (\epsilon - E_l)\dot{u}_l(r, E_l) + \mathcal{O}((\epsilon - E_l)^2), \tag{4.14}$$

the true radial function can be approximated sufficiently. The error in the band energies will be of the order $\mathcal{O}((\epsilon - E_l)^4)$. The energy derivatives can acquired from (4.5), taking the energy derivative:

$$\left\{-\frac{\hbar^2}{2m}\frac{\partial^2}{\partial r^2} + \frac{\hbar^2}{2m}\frac{l(l+1)}{r^2} + V(r) - E_l\right\} r\dot{u}_l(r) = r u_l(r). \tag{4.15}$$

The basis functions are now

$$\phi_{\mathbf{k}+\mathbf{G}}(\mathbf{r}) = \begin{cases} \frac{1}{\sqrt{\Omega}} e^{i(\mathbf{k}+\mathbf{G})\mathbf{r}} & \mathbf{r} \in \mathrm{IS} \\ \sum_{l=0}^{l_{max}} \sum_{m=-l}^{l} [a_{lm}^{\alpha}(\mathbf{k}+\mathbf{G}) u_l(r, E_l) + & \\ \qquad b_{lm}^{\alpha}(\mathbf{k}+\mathbf{G}) \dot{u}_l(r, E_l)]\, Y_{lm}(\hat{\mathbf{r}}) & \mathbf{r} \in \mathrm{MT}_\alpha. \end{cases} \tag{4.16}$$

Analogous to the APW method, the muffin-tin coefficients are determined as

$$\begin{aligned} a_{lm}^{\alpha}(\mathbf{K}) &= e^{i\mathbf{K}\mathbf{S}_\alpha} \frac{4\pi i^l}{W} Y_{lm}^*(\mathcal{U}_\alpha \hat{\mathbf{K}}) \\ &\quad [\dot{u}_l(R_\alpha) K j_l'(KR_\alpha) - \dot{u}_l'(R_\alpha) j_l(KR_\alpha)] && (4.17) \\ b_{lm}^{\alpha}(\mathbf{K}) &= e^{i\mathbf{K}\mathbf{S}_\alpha} \frac{4\pi i^l}{W} Y_{lm}^*(\mathcal{U}_\alpha \hat{\mathbf{K}}) \\ &\quad [u_l(R_\alpha) K j_l'(KR_\alpha) - u_l'(R_\alpha) j_l(KR_\alpha)] && (4.18) \end{aligned}$$

with the Wroskian

$$W = [\dot{u}_l(R_\alpha) u_l'(R_\alpha) - u_l(R_\alpha) \dot{u}_l'(R_\alpha)]. \tag{4.19}$$

Collecting terms equivalent to the APW basis set, with the definitions

$$\begin{aligned} A_{lm}^{i,\alpha}(\mathbf{k}) &= \sum_{\mathbf{G}} C_{\mathbf{k}+\mathbf{G}}^{i} \cdot a_{lm}^{\alpha}(\mathbf{k}+\mathbf{G}), \\ B_{lm}^{i,\alpha}(\mathbf{k}) &= \sum_{\mathbf{G}} C_{\mathbf{k}+\mathbf{G}}^{i} \cdot b_{lm}^{\alpha}(\mathbf{k}+\mathbf{G}) && (4.20) \end{aligned}$$

the wavefunctions take the form

$$\psi_i(\mathbf{k},\mathbf{r}) = \begin{cases} \frac{1}{\sqrt{\Omega}} \sum_{\mathbf{G}} C^i_{\mathbf{k}+\mathbf{G}} e^{i(\mathbf{k}+\mathbf{G})\mathbf{r}} & \mathbf{r} \in \mathrm{IS} \\ \sum_{lm} \left[A^{i,\alpha}_{lm}(\mathbf{k}) u_l(r, E_l) + B^{i,\alpha}_{lm}(\mathbf{k}) \dot{u}_l(r, E_l) \right] Y_{lm}(\hat{\mathbf{r}}) & \mathbf{r} \in \mathrm{MT}_\alpha \end{cases} \tag{4.21}$$

The detailed construction of the $\mathcal{H}$ and $\mathcal{S}$ matrices is described in [Kur00].

With this additional flexibility, the LAPWs form a good basis for most setups. In contrast to the APW method only one diagonalisation is needed to obtain the band energies. And since it is very unlikely that both radial function and its derivative vanish the asymptote problem does not occur.

Basis conversion: A method to link the simplicity of the planewave basis with the accuracy of the more sophisticated LAPW basis set has been proposed by Krasovskii [KSS99]. In this *Augmented Fourier components method* (AFC), the vicinity of the core containing rapid alterations of the wavefunctions is considered to be of low influence on the chemical behaviour. The results of calculation in LAPW basis are therefore *gauged* by an appropiate function, generating a smoother wavefunction in this region and leaving a slowly varying valence charge, which can be represented adequately in a planewave basis. From this results, quantities can be calculated in the simple planewave formalism.

4.4 The Local Orbital extension

There might be situations where the variational freedom of the LAPW basis set is not sufficient. One example are semi-core states, which are states of low energy thatdo not decay completely within the muffin-tins, but have an overlap into the interstitial. Singh [Sin91] introduced the *Local Orbital* extension to the LAPW set to deal with such problems.

The idea is to expand the basis set by additional functions that are zero in the interstitial, to extend flexibility inside the muffin-tins. By construcing these additional basis functions such that the derivative vanishes on the sphere boundaries as well, the A- and B- coefficients constructed in (4.17) remain unchanged. The new basis function should have the characteristic of a certain angular momentum l_{lo} and energy E_{lo}. This is ensured by a combination of three radial wavefunctions,

$$\phi_{lo} \sim [a^\alpha_{lo} u^\alpha_l(r, E_l) + b^\alpha_{lo} \dot{u}^\alpha_l(r, E_l) + c^\alpha_{lo} u^\alpha_l(r, E_{lo})]. \tag{4.22}$$

Here the index $lo = 1, \ldots, n_{lo}$ runs over the number of local orbitals introduced, the a_{lo}, b_{lo}, c_{lo} are the corresponding coefficients for each atom. The $l = l_{lo}$ indicates the angular momentum quantum number associated with this local orbital. This construction contains the essential characteristics in the third part

$(l(lo), E_{lo})$, enriched with the LAPW-like first two parts ensuring the conditions of the boundary.

These two conditions together with the normalization condition determine the a, b, c coefficients of each local orbital (for details on this, as well as on the construction of the matrix elements, see [Kur00]). The basis functions have to sitisfy Bloch's theorem. They are therefore matched to fictitious planewaves to obtain the proper XXX

4.5 Notes on symmetry

symmetries can be used to simplify the calculations.

... (as well as the other quantities like charge density and potentials)

- point group symmetry and space group symmetry.
- inversion symmetry: real and complex

$$C\text{real!} \tag{4.23}$$

equivalent atoms

4.6 Notes on the kinetic energy operator

Chapter 5

Implementation

The implementation of the dielectric function for this thesis has been done with the FLEUR code [FLE] in bulk mode. FLEUR is a full-potential linear augmented plane-wave (FLAPW) code. In the following sections some details of this implementation shall be discussed.

Since the linearized augmented plane-waves are the basis of choice, the formulae of the momentum matrix elements in this basis are presented in section 5.1. Details on performing the k-space integration to obtain the real part of the dielectric function are shown in 5.2. The real part is obtained in 5.3. Due to a restriction of FLEUR, the effect of backfolding has to be discussed in section 5.4. The problematic influence of this backfolding on the numerical integration is described in section 5.5. Some remarks in 5.6 are followed by a two test calculations.

When referring in the following to the dielectric function, often it's imaginary part is meant. This should be clear from the context.

5.1 Momentum matrix elements in the LAPW basis

The momentum matrix elements (MMEs)[1]

$$\frac{\hbar}{i}\langle f\mathbf{k}|\nabla|\imath\mathbf{k}\rangle = \frac{\hbar}{i}\int\limits_{uc} d^3r\ \psi_f^*(\mathbf{k},\mathbf{r})\nabla\psi_\imath(\mathbf{k},\mathbf{r}) \equiv M_{fi}(\mathbf{k}) \tag{5.1}$$

are to be calculated in the LAPW basis. Due to the partitioning of the unit cell into muffin-tins and the interstitial region by the choice of the augmented basis,

---

[1] To avoid confusion with the imaginary unit i, the initial electronic transition level is labeled $\imath$.

the matrix elements have to be calculated in these regions separately:

$$\langle\nabla\rangle = \langle\nabla\rangle_{IS} + \sum_{\alpha}\langle\nabla\rangle_{MT_\alpha}. \tag{5.2}$$

The formulae are presented in atomic units (see appendix C), so the factor $\hbar = 1$ disappears.

5.1.1 Interstitial contribution

In the interstitial, the wavefunctions are[2]

$$|\imath\mathbf{k}\rangle_{IS} = \frac{1}{\Omega}\sum_{\mathbf{G}} C^{\imath}_{\mathbf{k}+\mathbf{G}} e^{i(\mathbf{k}+\mathbf{G})\mathbf{r}}, \quad \mathbf{r}\in IS, \tag{5.3}$$

and the nabla operator acts like

$$\nabla|\imath\mathbf{k}\rangle = \frac{1}{\Omega}\sum_{\mathbf{G}} i(\mathbf{k}+\mathbf{G}) C^{\imath}_{\mathbf{k}+\mathbf{G}} e^{i(\mathbf{k}+\mathbf{G})\mathbf{r}}, \quad \mathbf{r}\in IS, \tag{5.4}$$

so that the interstitial part of the matrix element reads

$$\langle f\mathbf{k}|\tfrac{\nabla}{i}|\imath\mathbf{k}\rangle_{IS} = \frac{1}{\Omega}\sum_{\mathbf{G}\mathbf{G}'}(\mathbf{k}+\mathbf{G}) C^{f*}_{\mathbf{k}+\mathbf{G}'} C^{\imath}_{\mathbf{k}+\mathbf{G}} \int_{IS} d^3r\; e^{i(\mathbf{G}-\mathbf{G}')\mathbf{r}}. \tag{5.5}$$

The non-trivial interstitial volume the integral acts on is handled by subtracting the muffin-tins from the whole unit cell Ω:

$$\int_{IS} d^3r\; e^{i(\mathbf{G}-\mathbf{G}')\mathbf{r}} = \int_{\Omega} d^3r\; e^{i(\mathbf{G}-\mathbf{G}')\mathbf{r}} - \sum_{\alpha}\int_{MT_\alpha} d^3r\; e^{i(\mathbf{G}-\mathbf{G}')\mathbf{r}}. \tag{5.6}$$

While the first integral gives the simple value $\Omega\delta_{\mathbf{G}\mathbf{G}'}$, the integral over a muffin-tin centered at $\mathbf{S}_\alpha$ gives the split solution

$$\int_{MT_\alpha} d^3r\; e^{i(\mathbf{G}-\mathbf{G}')\mathbf{r}} = \begin{cases} V & \mathbf{G}=\mathbf{G}' \\ 3V_\alpha\frac{\sin x - x\cos x}{x^3}\cdot e^{i(\mathbf{G}-\mathbf{G}')\mathbf{S}_\alpha} & \mathbf{G}\neq\mathbf{G}' \end{cases} \tag{5.7}$$

with $x = |\mathbf{G}-\mathbf{G}'|R_\alpha$ and R_α, V_α the radius and the volume, respectively, of sphere α. Altogether this gives

$$\begin{aligned} \langle f\mathbf{k}|\tfrac{\nabla}{i}|\imath\mathbf{k}\rangle_{IS} &= \frac{1}{\Omega}\sum_{\mathbf{G}}(\mathbf{k}+\mathbf{G})\Bigg[C^{\imath}_{\mathbf{k}+\mathbf{G}}\Big(\Omega-\sum_{\alpha}V_\alpha\Big) - \\ &\qquad \sum_{\mathbf{G}'\neq\mathbf{G}} C^{f*}_{\mathbf{k}+\mathbf{G}'}\sum_{\alpha}3V_\alpha\frac{\sin x - x\cos x}{x^3}\cdot e^{i(\mathbf{G}-\mathbf{G}')\mathbf{S}_\alpha}\Bigg] && (5.8) \\ &= \sum_{\mathbf{G}\mathbf{G}'}(\mathbf{k}+\mathbf{G})C^{\imath}_{\mathbf{k}+\mathbf{G}}C^{f*}_{\mathbf{k}+\mathbf{G}'}\cdot s(\mathbf{G}-\mathbf{G}'). && (5.9) \end{aligned}$$

---

[2] For convenience, the general Ket symbol is used in place of its spatial representation.

In the last line, the expressions of the preceeding integral were merged into the function s, that is

$$s(\mathbf{G}-\mathbf{G}') = \begin{cases} \frac{1}{\Omega}(\Omega - \sum\limits_{\alpha} V_\alpha) & \mathbf{G}=\mathbf{G}' \\ -\frac{3}{\Omega}\sum\limits_{\alpha} V_\alpha \frac{\sin x - x\cos x}{x^3} e^{i(\mathbf{G}-\mathbf{G}')\mathbf{S}_\alpha} & \mathbf{G}\neq\mathbf{G}' \end{cases} \tag{5.10}$$

with the above $x = |\mathbf{G}-\mathbf{G}'|R_\alpha$. This is the Fourier representation of the step-function

$$S(\mathbf{r}) = \begin{cases} 1, & \mathbf{r}\in IS \\ 0, & \mathbf{r}\in MT, \end{cases} \tag{5.11}$$

which is usually constructed already for the construction of the Hamilton and overlap matrices $\mathcal{H}$ and $\mathcal{S}$ in the self-consistency part.

5.1.2 Muffin-tin contributions

The further procedure depends on what form of wavefunctions you start from. If you use the LAPW functions written explicitly in the basis functions (4.16), without the summation (4.20) in the calculation of your MMEs (5.1), you obtain the summations over $\mathbf{G}$,l,m each twice. In the further derivation, not only one pair of the (l,m)-summation vanishes, but also, by clever conversion, the second m-summation [Kra]. This leaves summations $\mathbf{G},\mathbf{G}',l$. If you do this, you can simply check the hermiticity of your matrix for every $\mathbf{G}$-vector.

In the derivation used in this thesis, LAPWs of the accumulated form (4.21) are used. To derive the matrix elements in the spheres, the momentum operator is expressed in spherical coordinates, and its impact on the spherical harmonics is calculated. Since this part is a bit lengthy, it is moved to appendix A.

In allusion to the ladder operators L_+ and L_- of the angular momentum operator, one expresses the momentum matrix elements not in terms of $(\partial x, \partial y, \partial z)^T$, but in the rotated form

$$\begin{pmatrix} \partial x + i\partial y \\ \partial x - i\partial y \\ \partial z \end{pmatrix} = \mathcal{M} \begin{pmatrix} \partial x \\ \partial y \\ \partial z \end{pmatrix} \equiv \begin{pmatrix} \partial_1 \\ \partial_2 \\ \partial_3 \end{pmatrix}, \tag{5.12}$$

with the base change matrix and its inverse

$$\mathcal{M} = \begin{pmatrix} 1 & i & 0 \\ 1 & -i & 0 \\ 0 & 0 & 1 \end{pmatrix}, \quad \mathcal{M}^{-1} = \begin{pmatrix} \frac{1}{2} & \frac{1}{2} & 0 \\ -\frac{1}{2}i & \frac{1}{2}i & 0 \\ 0 & 0 & 1 \end{pmatrix}. \tag{5.13}$$

The result contains only one (l, m)-summation can be expressed as

$$
\begin{array}{llcccll}
\multicolumn{7}{l}{\langle f\mathbf{k}|\partial_n|\imath\mathbf{k}\rangle = \displaystyle\sum_{l=0}^{l_{max}-1}\sum_{m=-l}^{l}} \\
 & [\,(\int u_{l+1}u'_l\; r^2dr & - & l & \int u_{l+1}u_l\; rdr) & A^{f*}_{l+1,m'}A^{\imath}_{l,m} & \\
+ & \;\;(\int u_{l+1}\dot{u}'_l\; r^2dr & - & l & \int u_{l+1}\dot{u}_l\; rdr) & A^{f*}_{l+1,m'}B^{\imath}_{l,m} & \\
+ & \;\;(\int \dot{u}_{l+1}u'_l\; r^2dr & - & l & \int \dot{u}_{l+1}u_l\; rdr) & B^{f*}_{l+1,m'}A^{\imath}_{l,m} & \\
+ & \;\;(\int \dot{u}_{l+1}\dot{u}'_l\; r^2dr & - & l & \int \dot{u}_{l+1}\dot{u}_l\; rdr) & B^{f*}_{l+1,m'}B^{\imath}_{l,m}\,] & F^{(2n-1)}_{l,m} \\
+ & [\,(\int u_l u'_{l+1}\; r^2dr & + & (l+2) & \int u_{l+1}u_l\; rdr) & A^{f*}_{l,m}A^{\imath}_{l+1,m''} & \\
+ & \;\;(\int u_l\dot{u}'_{l+1}\; r^2dr & + & (l+2) & \int u_{l+1}\dot{u}_l\; rdr) & A^{f*}_{l,m}B^{\imath}_{l+1,m''} & \\
+ & \;\;(\int \dot{u}_l u'_{l+1}\; r^2dr & + & (l+2) & \int \dot{u}_{l+1}u_l\; rdr) & B^{f*}_{l,m}A^{\imath}_{l+1,m''} & \\
+ & \;\;(\int \dot{u}_l\dot{u}'_{l+1}\; r^2dr & + & (l+2) & \int \dot{u}_{l+1}\dot{u}_l\; rdr) & B^{f*}_{l,m}B^{\imath}_{l+1,m''}\,] & F^{(2n)}_{l+1,m''}
\end{array}
\tag{5.14}
$$

for $n = 1, 2, 3$ indicating the components, and m',m'' given by

$$
m' = \begin{pmatrix} m+1 \\ m-1 \\ m \end{pmatrix}, \quad m'' = \begin{pmatrix} m-1 \\ m+1 \\ m \end{pmatrix} \quad \text{for} \quad n = \begin{pmatrix} 1 \\ 2 \\ 3 \end{pmatrix}. \tag{5.15}
$$

The factors $F^{(n)}_{lm}$ are defined in appendix A. In the combinations of coefficients owning angular quantum numbers l and $l+1$ in the products, one recognizes the dipole selection rules, i.e. the conservation of angular momentum.

The notation already indicates that only the large component of the wavefunction inside the muffin-tins is taken into account. For the valence states considered this is a good approximation. The contributions resulting from the local orbital extension to the LAPW basis set (**??**) are similar in shape to those of the simple LAPW basis (5.14), but more lengthy, and are hence given in appendix A as well.

5.1.3 Properties of the matrix elements

Hermiticity: Since the momentum operator is an observable and therewith hermitian, so must be its matrix elements. This can be shown easily by applying partial integration to the defining formula of the matrix elements (5.1). It is also obvious for the MMEs written in the plane-wave basis (4.4).

However it can be hardly seen from the formulae written in LAPW basis, since the interstitial plane-waves are expanded on the muffin-tin boundaries in terms of spherical harmonics utilizing the Rayleigh relation (4.8). If one applies partial integration to the LAPW formulae, one can see that e.g. for the $(x + iy)$-component of the muffin-tin contribution to the MME, parts of the factors containing $F^{(1)}_{l,m}$ compensate with the complex conjugate of the factors containing $F^{(2)}_{l+1,m-1}$, leaving the boundary values of the integration un-compensated.

The rest has to be taken by the difference in conjugating the interstitial contribution, which is sensitive to conjugation due to the factor $(\mathbf{k}+\mathbf{G})$ in the first sum in (5.9).

Reality: The diagonal matrix elements are real since the momentum operator is an observable. Furthermore this can also be seen from and compared with the derivatives of the energy bands (3.43). The non-diagonal parts are in general complex, as can be assumed because of the complex A,B muffin-tin coefficients. For the case of inversion symmetry, however, the matrix elements become real. This is obvious for the plane-wave basis (4.4) due to the now real C coefficients (4.23), but not for LAPW basis (due to the re-expansion on the muffin-tin boundaries).

Equivalent atoms: XXXX

Should be real for diagonal

In general complex, but ε_2 is real again!

'magic of numbers'

5.1.4 Illustration

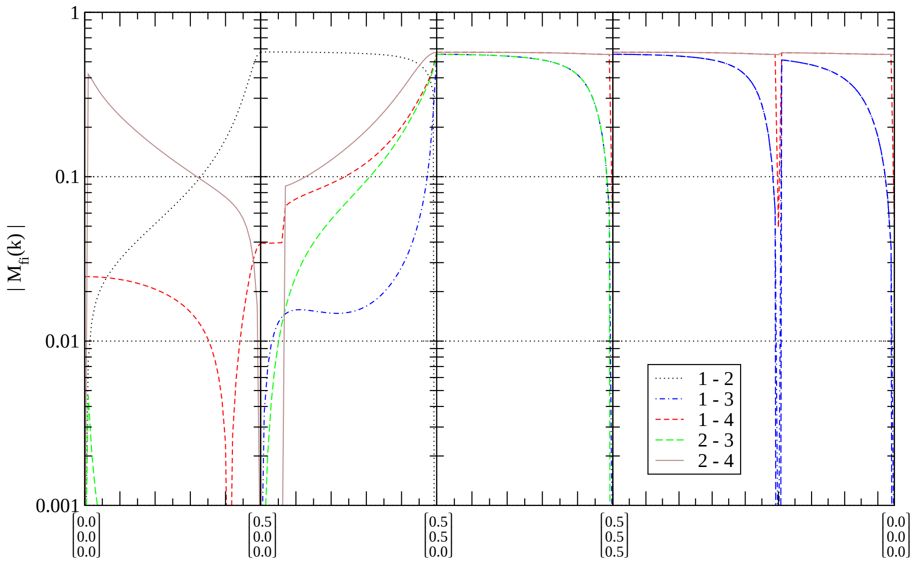

Figure 5.1: The absolute value of matrix elements for five selected transitions evolving on paths on the border of the irreducible Brillouin zone. The initial and final level $\imath$ and f are given in the legend.

To give an impression of the amplitude and k-dependence, a band structure-like plot of matrix elements is shown in figure 5.1. These are selected MMEs for a simple-cubic Aluminum setup with one atom per unit cell, that is investigated in section 5.4. The path is $(0,0,0) \rightarrow (\frac{1}{2},0,0) \rightarrow (\frac{1}{2},\frac{1}{2},0) \rightarrow (\frac{1}{2},\frac{1}{2},\frac{1}{2}) \rightarrow (0,0,0)$, and due to big variations in amplitude, the plot uses a logarithmic y-axis.

The progression of the curve is monotonous in most areas. On the corners of the path, the matrix elements are not unique due to degeneracy (compare to the band structures in section 5.4). However, some transitions have a rapid change in amplitude when approaching the corners. In this case, only the sum over the transitions has a physical meaning and gives deterministic results. Another irregularity are jumps that occur within a path, which can usually be connected to band crossings.

5.2 k-space integration

The task to perform an integration in k-space

$$\frac{1}{V_G}\sum_i \int_{BZ} d^3k\ U(\mathbf{k})f(\epsilon_i(\mathbf{k})) \tag{5.16}$$

(V_G being the volume of the Brillouin zone, f the Fermi factor at temperature zero, i.e. a step function) frequently appears in band structure calculations, for instance in the determination of the Fermi energy in the self-consistency of the density functional theory described in section 2.3. The integrand $U(\mathbf{k})$ is calculated only for a very finite set of sample k-points.

There are different kinds of methods, e.g. the special points method [CC73, Cun74]. It provides a set of special k-points in the irreducible Brillouin zone with alleged weights to calculate the integrand on. This transfers the integration (5.16) into a summation

$$\frac{1}{V_G}\sum_i \int_{BZ} d^3k\ U(\mathbf{k})f(\epsilon_i(\mathbf{k})) \rightarrow \sum_i \sum_{\mathbf{k}} U(\mathbf{k}) w_{i\mathbf{k}}. \tag{5.17}$$

For smoothly varying functions this yields reliable results. However, for incomplete occupied bands the integrand in (5.16) is not smooth due to the sharp Fermi factor. Consider for instance a band close to the Fermi energy. In the self-consistency, this band could be shifted above or below the Fermi energy, resulting in big changes in the charge density. This can degrade or even destroy the convergence. One can implement a more elaborate Fermi factor like the true Fermi function

$$f(\epsilon) = e^{\frac{e-E_F}{kT}} - 1, \tag{5.18}$$

that is making the integrand smoothly by a *temperature broadening.*

Another method of integration is to divide the volume into subvolumes of a certain shape and perform the integration in the volume analytically over the interpolated function. Among the method of Gilat and Raubenheimer [GR66, Bro93], the *Tetrahedron Method* is the most prominent integration method of this kind.

Tetrahedra: This method was introduced independently by Lehmann and Taut [LT72] in 1972 and by Andersen and Jepsen [JA71] in 1971. It's idea is to divide the integration volume into tetrahedra. This is always possible, though not uniquely. The tetrahedra can in principle have arbitrary shape, but ought to be as regular in shape as possible (e.g. not flattened). The integration thus changes to

$$\frac{1}{V_G}\int_{BZ} d^3k \quad \rightarrow \quad \sum_{\{Tet\}} \frac{V_T}{V_G}\int_{V_T} d^3k\ . \tag{5.19}$$

V_T is the tetrahedron's volume. In each tetrahedron, the energy interpolated linearly is given uniquely by the four corner energies.

Interpolation in one tetrahedron: The corners are labeled from 0 to 3 with increasing energy, i.e.

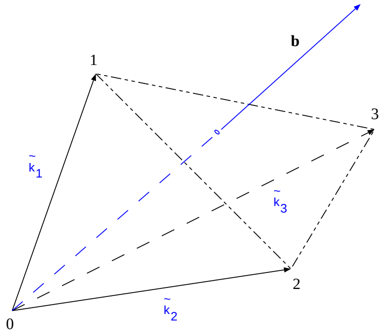

Figure 5.2: A tetrahedron with corner labels sorted by energy, and interpolation vector **b**. The small circle marks the penetration point of the vector.

$$\epsilon_0 < \epsilon_1 < \epsilon_2 < \epsilon_3. \tag{5.20}$$

For equally indicated k-vectors, the energy in linear interpolation is

$$\epsilon(\mathbf{k}) = \epsilon_0 + \mathbf{b}\cdot(\mathbf{k} - \mathbf{k}_0). \tag{5.21}$$

Here, the vector $\mathbf{b}$ is defined just that the energy coincides for k equal $\mathbf{k}_0, \mathbf{k}_1, \mathbf{k}_2, \mathbf{k}_3$ with the given corner energies. This is provided with the definition

$$\mathbf{b} = \sum_{i=1}^{3} (\epsilon_i - \epsilon_0)\mathbf{r}_i, \tag{5.22}$$

including the auxiliary vectors

$$\begin{aligned} \tilde{\mathbf{k}}_i &= \mathbf{k}_i - \mathbf{k}_0, \qquad i \in \{1,2,3\} && (5.23) \\ \mathbf{r}_i &= \frac{1}{V_T} \tilde{\mathbf{k}}_j \times \tilde{\mathbf{k}}_k, \quad \{i,j,k\} \text{ cyclic.} && (5.24) \end{aligned}$$

This interpolation yields a continuous energy in the whole integration volume BZ made out of the set of tetrahedra. The integrand can be interpolated analogously like

$$U(\mathbf{k}) = U_0 + \mathbf{b}' \cdot (\mathbf{k} - \mathbf{k}_0) \tag{5.25}$$

with the according definition

$$\mathbf{b}' = \sum_{i=1}^{3} (U_i - U_0)\mathbf{r}_i. \tag{5.26}$$

With this the whole integrand is continuous in the integration volume. A possible simplification is to take the integrand set to a constant value $\bar{U}$ averaged over the tetrahedron. With this, the quantity is of course not continuous anymore.

Given this linear form of the integrand, the integration in each tetrahedron can be performed analytically.

Spectral calculations: This method works fine for spectral integrals (for instance those kinds of integrals mentioned in section 3.3. Take integrals of the type of the density-of-states

$$\begin{aligned} D(E) &= \frac{1}{V_G} \sum_i \int_{BZ} d^3k \; \delta(E - E_i(\mathbf{k})) \\ &= \frac{1}{V_G} \sum_i \int_{E=E_i(\mathbf{k})} dS \; \frac{1}{|\nabla_{\mathbf{k}} E_i(\mathbf{k})|}. \end{aligned} \tag{5.27}$$

If this integrand is interpolated linearly like in (5.25), it gives

$$\frac{1}{|\nabla_{\mathbf{k}} E(\mathbf{k})|} = \frac{1}{|\mathbf{b}|}. \tag{5.28}$$

The constant-energy plane $E = E_i(\mathbf{k})$ in one tetrahedron is the cross-section of a plane perpendicular to $\mathbf{b}$. There are three possible case of this plane to cut the tetrahedron, yielding a cutting area A and leading to a contribution of the integral equal $\frac{A}{|\mathbf{b}|}$. The explicit results are [LT72]

$$D_T(\epsilon) = \begin{cases} 0 & \epsilon < \epsilon_1 \text{ or } \epsilon_4 < \epsilon \\ \frac{V_T}{V_G} \frac{3(\epsilon-\epsilon_1)^2}{\epsilon_{21}\epsilon_{31}\epsilon_{41}} & \epsilon_1 < \epsilon < \epsilon_2 \\ \frac{V_T}{V_G} \frac{1}{\epsilon_{31}\epsilon_{41}} \left[3\epsilon_{21} + 6(\epsilon - \epsilon_2) - 3\frac{(\epsilon_{31}+\epsilon_{42})(\epsilon-\epsilon_2)^2}{\epsilon_{32}\epsilon_{42}} \right] & \epsilon_2 < \epsilon < \epsilon_3 \\ \frac{V_T}{V_G} \frac{3(\epsilon_4-\epsilon)^2}{\epsilon_{41}\epsilon_{42}\epsilon_{43}} & \epsilon_3 < \epsilon < \epsilon_4 \end{cases} \tag{5.29}$$

with the energy differences $\epsilon_{ij} = \epsilon_i - \epsilon_j$.

Inclusion of Fermi factors: If unlike (5.27) the integral contains a Fermi factor like (5.16) which is simply included into the integrand, the described proceeding will not give good results since the values are possibly interpolated to zero because of this factor. But due to the linear interpolation, energy cross-sections are easy to determine, as done for the density of states. Nothing else is a Fermi factor that separates the occupied and unoccupied part by a constant-energy plane.

For in integral (5.16), depending on the energy ϵ and the Fermi energy ϵ_F referring to, the valid contribution can consist out zero volume ($\epsilon_F < \epsilon_1$), one subtetrahedron ($\epsilon_1 < \epsilon_F < \epsilon_2$), three subtetrahdra ($\epsilon_2 < \epsilon_F < \epsilon_3$ or $\epsilon_3 < \epsilon_F < \epsilon_4$), or the complete tetrahedron ($\epsilon_4 < \epsilon_F$) [RF75].

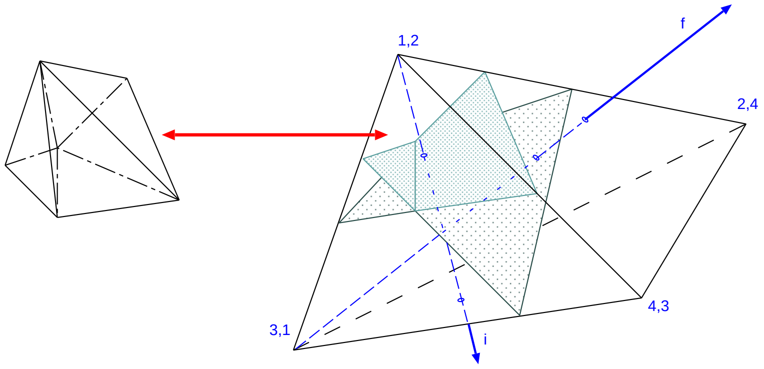

Figure 5.3: A tetrahedron that is divided due to two Fermi factors. The numbers at the corners are the sorted energy indices for the initial and final bands $\imath$ and f, the two vectors are the corresponding $\mathbf{b}$ vectors (5.22). In this diagram the energy cuts both bands within the tetrahedron and results in two crossing constant-energy planes. Cutting of vectors with these planes or the tetrahedra boundary are marked with small circles. The valid subvolume is marked with the red arrow, as well as shown on the left, with its division into three subtetrahedra.

For an integral containing two Fermi factors like (3.39), one performs on each subtetradron obtained for the first Fermi factor the (inverse) occupation procedure for the second Fermi factor, resulting in at most nine subtetrahedra for the initial tetrahedron. Note that for the second step a renumbering has to be made due to the possibly different order of the energies E_f.

For the integration (3.39), this means that for every transition $\imath \to f$, the valid volume is determined, and the remaining integrand, i.e.

$$U(\mathbf{k}) = \frac{\langle \imath\mathbf{k}|p_\alpha|f\mathbf{k}\rangle\langle f\mathbf{k}|p_\beta|\imath\mathbf{k}\rangle}{|\nabla_\mathbf{k}(E_f(\mathbf{k}) - E_\imath(\mathbf{k}))|}, \tag{5.30}$$

is evaluated for each of the valid volume's tetrahedra.

Weighted formulation: Blöchl has shown that the tetrahedron method can also be written to result in the form of a weighted summation (5.17). These weights are given in appendix B. With this formalism, arbitrary functions can be integrated without doing the geometric derivation done for instance in the formulae of the density-of-states above.

It should be noted that the obtained weights do not coincide with those of the special point method which are based on symmetry, i.e. the tetrahedron method does not take into account the high symmetry character of the irreducible zone's boundaries. This leads to a worse convergence than using the special points method, and is the reason why the tetrahedron method is usually not used for the self-consistency, but for spectral calculations.

Attempts have been made to raise the level of interpolation to a quadratic one. When marking out such a formalism to the linear one introduced above, the latter one is referred to explicitly as *linear tetrahedron* (LT) method.

Reduction to the Irreducible Brillouin Zone (IBZ): Usually the eigenvectors and eigenvalues are calculated only in the irreducible part of the Brillouin zone. Let's consider the effect on integral (3.39). Let $\mathcal{R}$ be an appropriate rotation matrix. The energies are the same at the rotated k-point

$$E_\imath(\mathbf{k}) = E_\imath(\mathcal{R}\mathbf{k}), \tag{5.31}$$

but the eigenvectors are rotated:

$$\langle \mathbf{r}|\imath, \mathcal{R}\mathbf{k}\rangle = \langle \mathcal{R}^{-1}\mathbf{r}|\imath, \mathbf{k}\rangle \tag{5.32}$$

For the calculation of the momentum matrix elements, instead of rotating the eigenvectors one can also rotate the coordinate system and therewith the nabla operator, in symbols $\nabla_{\mathcal{R}\mathbf{r}} = \mathcal{R}\nabla_\mathbf{r}$. With this the matrix element for a k-point $\mathcal{R}\mathbf{r}$

in the first Brillouin zone, but outside the irreducible wedge, can be computed like

$$\begin{aligned}
\langle f, \mathcal{R}\mathbf{k}|\nabla|\imath, \mathcal{R}\mathbf{k}\rangle &= \int d^3r \; \psi_f^*(\mathcal{R}\mathbf{k}, \mathbf{r}) \; \nabla_{\mathbf{r}} \; \psi_\imath(\mathcal{R}\mathbf{k}, \mathbf{r}) \\
&= \int d^3r \; \psi_f^*(\mathbf{k}, \mathcal{R}^{-1}\mathbf{r}) \; \nabla_{\mathbf{r}} \; \psi_\imath(\mathbf{k}, \mathcal{R}^{-1}\mathbf{r}) \\
&= \int d^3r \; \psi_f^*(\mathbf{k}, \mathbf{r}) \; \nabla_{\mathcal{R}\mathbf{r}} \; \psi_\imath(\mathbf{k}, \mathbf{r}) \\
&= \mathcal{R}\langle f\mathbf{k}|\nabla|\imath\mathbf{k}\rangle \qquad (5.33)
\end{aligned}$$

When calculating the integral

$$\varepsilon_2^{\alpha\beta}(\omega) \sim \sum_{\imath f} \int_{\hbar\omega=\Delta E}^{BZ} dS \frac{\langle \imath\mathbf{k}|\nabla_\alpha|f\mathbf{k}\rangle^\dagger \langle f\mathbf{k}|\nabla_\beta|\imath\mathbf{k}\rangle}{|\nabla_{\mathbf{k}}(E_f(\mathbf{k}) - E_\imath(\mathbf{k}))|} f(E_\imath(\mathbf{k}))[1 - f(E_f(\mathbf{k}))] \quad (5.34)$$

with only use of the irreducible part, one uses the identity of the energies at the corresponding k-points (5.31). Furthermore $\mathcal{R}^\dagger = \mathcal{R}^{-1}$, so that the numerator of the fraction in the preceding integral gives

$$\langle \imath, \mathcal{R}\mathbf{k}|\nabla_\alpha|f, \mathcal{R}\mathbf{k}\rangle^\dagger \langle f, \mathcal{R}\mathbf{k}|\nabla_\beta|\imath, \mathcal{R}\mathbf{k}\rangle = \langle \imath\mathbf{k}|\nabla_\alpha|f\mathbf{k}\rangle^\dagger \langle f\mathbf{k}|\nabla_\beta|\imath\mathbf{k}\rangle \quad (5.35)$$

and the integral itself

$$\varepsilon_2^{\alpha\beta}(\omega) \sim N_{\mathcal{R}} \sum_{\imath f} \int_{\hbar\omega=\Delta E}^{IBZ} dS \frac{\langle \imath\mathbf{k}|\nabla_\alpha|f\mathbf{k}\rangle^* \langle f\mathbf{k}|\nabla_\beta|\imath\mathbf{k}\rangle}{|\nabla_{\mathbf{k}}(E_f(\mathbf{k}) - E_\imath(\mathbf{k}))|} f(E_\imath(\mathbf{k}))[1 - f(E_f(\mathbf{k}))] \quad (5.36)$$

with $N_{\mathcal{R}}$ the number of symmetry operations.

A note on cubic systems: Since we know from section three that the dielectric tensor has unit form for cubic crystals, one can immediately reduce the calculation (5.36) to the scalar case, using the square of the absolute value in the numerator.

This is not to be mixed up with the momentum matrix elements itself, which of course still have independent components. For instance remember the diagonal MMEs being proportional to the band derivatives, which have a well-defined direction.

Reality: The imaginary part of the dielectric function $\varepsilon_2(\omega)$ is a real function. So must be the results of (5.36). For the cubic case this is obvious since the denominator reduces to a real expression.

In the case of non-cubic systems (3.39), the integral contains products of momentum matrix elements $M_{\imath f}^{\alpha *} M_{f\imath}^{\beta}$ which are in general complex. This means that the components of the tensor obtained from (5.36) can be complex, obeying the relation $\varepsilon_2^{\alpha\beta} = \varepsilon_2^{\beta\alpha *}$. But according to (3.40), the resulting dielectric function along a unit vector $\mathbf{u}$ is composed of a summation

$$\varepsilon_2 = \sum_{\alpha,\beta} \varepsilon_2^{\alpha\beta} u_\alpha u_\beta, \tag{5.37}$$

containing for every contribution of $\varepsilon_2^{\alpha\beta}$ the transposed part $\varepsilon_2^{\beta\alpha}$ as well. Therefore the dielectric function ε_2 becomes real, and one can reduce the dielectric tensor to its real part $\tilde{\varepsilon}_2 = \Re\varepsilon_2$ (i.e. symmetrizing it by $(\tilde{\varepsilon}_2^{\alpha\beta} = \frac{1}{2}(\varepsilon_2^{\alpha\beta} + \varepsilon_2^{\beta\alpha}))$. This also restores consistency with the statement in chapter 3 that the dielectric tensor is symmetrical.

5.3 The Real part of the Dielectric Function

Due to the tight relation between real (3.28) and imaginary part (3.29) of spectral functions, one can set up a formula for the real part similar to (3.39) containing a k-space integration. This has been done e.g. for the magnetic susceptibility by Gilat and Bharatiya [GB75]. They used the tetrahedron integration scheme to derive analytical expressions for the integral contributions that are quite lengthy.

In this thesis, the alternative path is followed, i.e. the Kramers-Kronig integration transformation (3.32) is employed.

Numerical accuracy of the Kramers-Kronig relations: The accuracy of the applied integration should be tested on a prominent analytical example, this is the harmonic oscillator. The real and imaginary part are given by

$$\varepsilon_1(\omega) = 1 + \frac{N_0 e^2}{m} \frac{(\omega_0^2 - \omega^2)}{(\omega_o^2 - \omega^2)^2 + \omega^2\delta^2} \tag{5.38}$$

$$\varepsilon_2(\omega) = \frac{N_0 e^2}{m} \frac{\omega\delta}{(\omega_o^2 - \omega^2)^2 + \omega^2\delta^2}. \tag{5.39}$$

The functions are plotted in figures 5.4 and 5.5 for two different attenuations $\delta = 0.2$ and $\delta = 1.0$, furthermore: $N_0 e^2/m = 1$, $\omega_{max} = 10\frac{1}{s}$, $\omega_0 = 4.5\frac{1}{s}$. The analytical solutions are plotted in thick black, while the numerical solutions of the real part are plotted dashed blue. Numerical solutions are given for three different number of sampling points, 100, 400, 1000, and 25000 (in the second plot only).

One can see that there is a need for an appropriate set of mesh points (in the order of thousand or more) to achieve a numerical curve close to the analytic one. The first region of problem of these curves is at the extrema close to ω_0, where the numerical solution slowly converges to the analytic one. The second problematic energy range is for energies close to zero. There is a discrepancy raising with the attenuation δ that is not removed by a larger mesh point set.

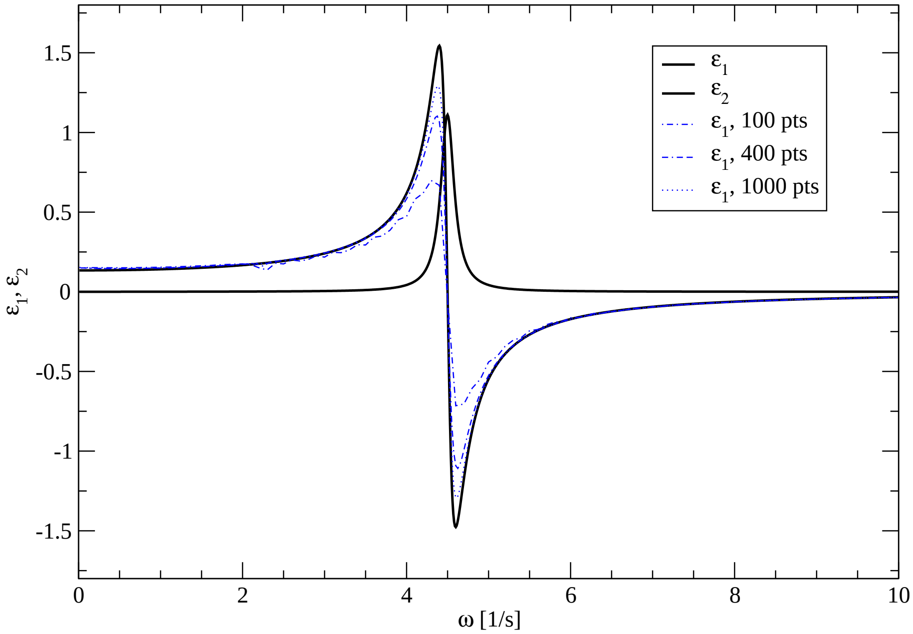

Figure 5.4: Analytic real and imaginary part for $\delta = 0.2$ (thick black lines) and numerical real part for different numbers of mesh points (blue lines).

5.4 Backfolding

At this point it should be mentioned that there are degrees of freedom in the choice of the unit cell. There might be unit cells of different shapes for the same number of atoms, resulting in a different reciprocal lattice. In doing so the band structure stays unchanged in the reciprocal space, but appears different due to the differently chosen basis. There is also the possibility and (possibly the need) to choose a bigger unit cell to model the system, giving a smaller Brillouin zone with modified bands.

The effect on the band structure, called *backfolding*, shall be discussed here. Since the dielectric properties are understood to be transitions between bands, understanding of the impact of backfolding is essential if dealing with bigger unit cells.

5.4.1 Algebraic considerations

To understand the effect of periodicity, the Bloch theorem should be recapitulated, to simplify matters in one dimension for a non-degenerate system including time-reversal symmetry. The Schrödinger equation

$$\mathcal{H}\psi_n(r) = E\psi_n(r) \tag{5.40}$$

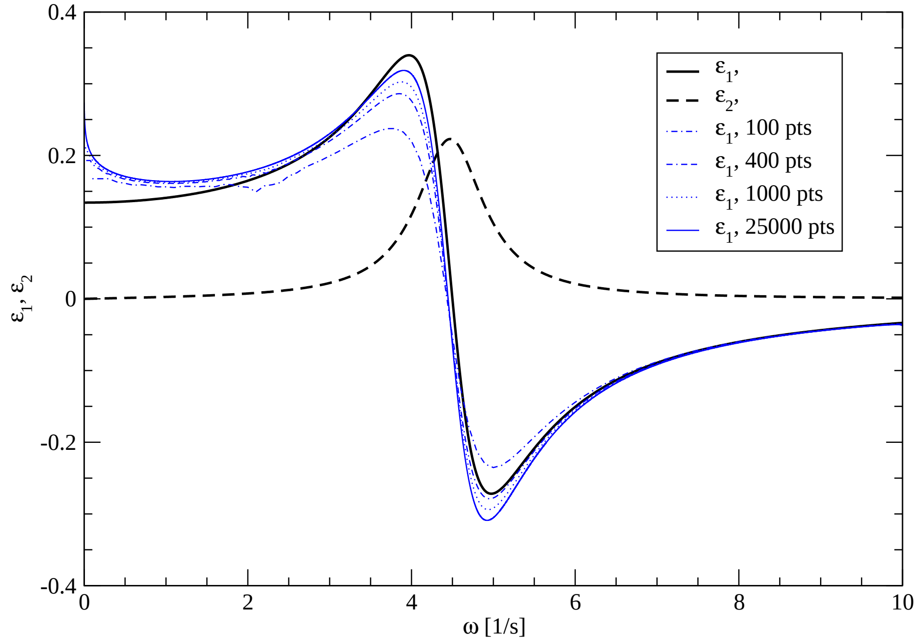

Figure 5.5: Analytic real and imaginary part for $\delta = 1.0$ (thick black lines) and numerical real part for different numbers of mesh points (blue lines).

yields eigenvalues E and eigenvectors ψ. When the system consists of unit cells of length R, the corresponding translation operator is defined as

$$\mathcal{T}_R : r \rightarrow r + R, \tag{5.41}$$

with the properties

$$\begin{aligned} [\mathcal{T}_R, \mathcal{H}] &= 0, && (5.42) \\ \mathcal{T}_R \psi_n(r) &= \psi_n(r + R). && (5.43) \end{aligned}$$

This translation operator shares a common set of eigenvectors with the Hamiltonian. Since the absolute square of the wavefunctions is independent under proper translations,

$$\mathcal{T}_R|\psi|^2 = \mathcal{T}_R(\psi^*\psi) = (\mathcal{T}_R^*\psi^*)(\mathcal{T}_R\psi) = |\lambda|^2|\psi|^2, \tag{5.44}$$

the eigenvalues of the translational operator take the form $\lambda = e^{ikr}$, which at the same time classifies the wavefunctions: $\psi_n(r) \rightarrow \psi_n(k, r)$. Furthermore, as a consequence of (5.42) these wavefunctions can be chosen to take *Bloch form*

$$\psi_n(k, r) = e^{ikR}\varphi_n(k, r), \quad \varphi_n(k, r) = \varphi_n(k, r + R), \tag{5.45}$$

consisting of an exponential and a lattice-periodic function. The essential clou now is how Bloch waves *shifted in k-space* react on translations in real space:

$$\mathcal{T}_R \psi_n(k+G,r) = e^{i(k+G)R}\psi_n(k+G,r) = e^{ikR}\psi_n(k+G,r). \tag{5.46}$$

This means that all shifted k-vectors $k+G$ are associated to the same eigenvalue $\lambda = e^{ikR}$ of the translation operator. Therefore the set of eigenvalues and eigenvectors at $k+G$ are *equivalent* to those at k. Therefore one can reduce all considerations to the first Brillouin zone $-\frac{K}{2} \leq k \leq \frac{K}{2}, K = \frac{2\pi}{L}$. One might be confused by this insight since the Hamiltonian in matrix representation in a basis seems to change with a substitution of k to $k+G$. For the case of an infinite basis this substitution only concerns permutations of rows and columns. For a finite basis, one gets numerical problems for high-lying states.

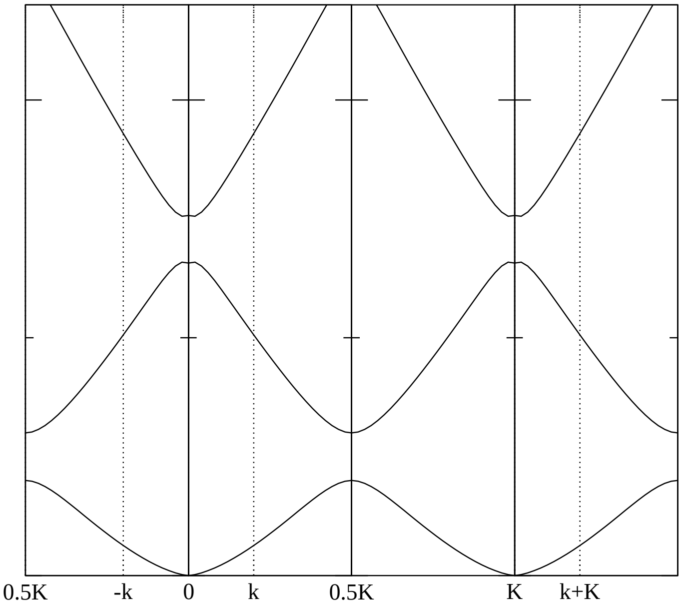

Figure 5.6: Sample band structure similar to nearly-free electrons. The First Brillouin zone's boundary is at $\frac{1}{2}K$. Two equivalent k-points to k are marked, $-k$ and $k+K$.

The consequence for the band structure is shown for a system similar to nearly-free electrons in figure 5.6. The solid vertical lines at $\frac{1}{2}K, K, \ldots$ are the boundaries of the Brillouin zones. The dashed lines indicate one k-point k and equivalents of it at $-k$ and $k+K$.

If one now imposes a lower periodicity like $\tilde{R} = 2R$, the reciprocal lattice and therewith the Brillouin zone reduces to half the size, $|k| \leq \tilde{K}, \tilde{K} = \frac{\pi}{L}$. A denser periodicity of $\tilde{K} = \frac{K}{2}$ is demanded now instead of K in the first place,

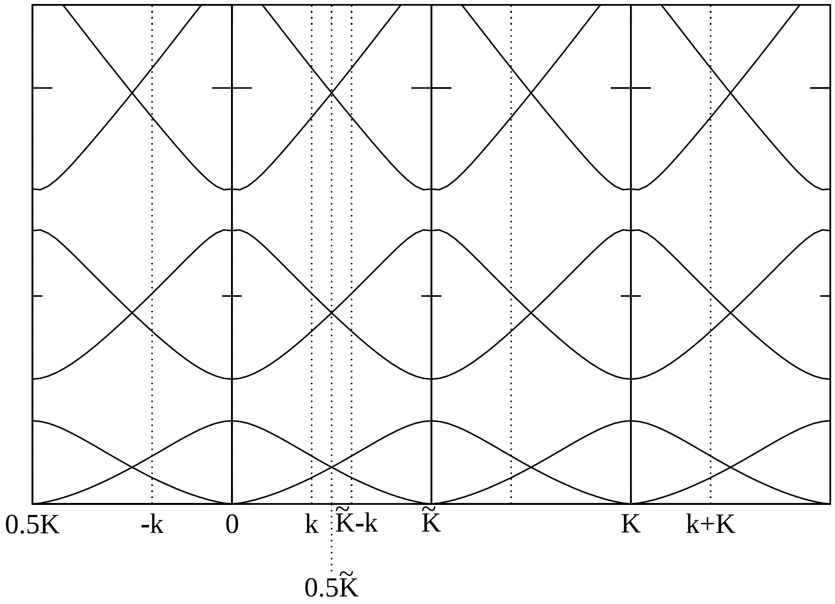

Figure 5.7: Sample band structure for a system for that a lower translational symmetry than in figure 5.6 has been used. The new Brillouin zone border is $\frac{1}{2}\tilde{K}$. Additionally, $\tilde{K} - k$ is marked as equivalent to k now.

with . This makes the point $-k$ (which is equivalent to k due to time-reversal) equivalent to $-k + \tilde{K} = \frac{K}{2} - k$. Since these two points have (possibly) distinct sets of eigenvalues in the initial setup of high periodicity, these two sets sum up in this setup.

The corresponding band structure is shown in figure 5.7. The periodicity of branches has been doubled, the first Brillouin zone shrinks to half the size $\tilde{K}$, and the number of bands in it doubled. This figure gives an idea of the origin of the term *backfolding.* The bands look folded back at the center of the former bigger Brillouin zone; but the superposition with an additional band structure is a better way to visualize.

5.4.2 Representation in a basis

The impact of backfolding on the energy eigenvalues has been shown in the previous paragraph. But the dielectric function essentially depends on the momentum matrix elements and therewith on the wavefunctions. Here, the effect of backfolding should be illustrated for a plane-wave calculation.

For simplicity, I choose a simple, hypothetical system of Aluminum (Al) in a simple cubic (sc) structure[3]. This is calculated in two setups ($\mathcal{A}$ denotes sets of

---

[3] So in this context, SC is not meant to be an abbreviation of *self-consistency*, as in the

basis vectors, $\mathcal{D}$ are atom positions in coordinates of these basis vectors)

$$\mathcal{A}_1 = \left\{ L\begin{pmatrix}1\\0\\0\end{pmatrix}, L\begin{pmatrix}0\\1\\0\end{pmatrix}, L\begin{pmatrix}0\\0\\1\end{pmatrix} \right\}, \quad \mathcal{D}_1 = \left\{ \begin{pmatrix}0\\0\\0\end{pmatrix} \right\} \tag{5.47}$$

and

$$\mathcal{A}_2 = \left\{ L\begin{pmatrix}1\\0\\0\end{pmatrix}, L\begin{pmatrix}0\\1\\0\end{pmatrix}, L\begin{pmatrix}0\\0\\2\end{pmatrix} \right\}, \quad \mathcal{D}_2 = \left\{ \begin{pmatrix}0\\0\\0\end{pmatrix}, \begin{pmatrix}0\\0\\\frac{1}{2}\end{pmatrix} \right\}, \tag{5.48}$$

that is the second setup doubles the first one in z-direction. The resulting reciprocal lattices (written in form of Bravais matrices, i.e. writing the (transposed) reciprocal basis vectors in matrix form) are

$$\mathcal{B}_1 = \frac{2\pi}{L}\begin{pmatrix}1&0&0\\0&1&0\\0&0&1\end{pmatrix}, \quad \mathcal{B}_2 = \frac{2\pi}{L}\begin{pmatrix}1&0&0\\0&1&0\\0&0&\frac{1}{2}\end{pmatrix}, \tag{5.49}$$

the second setup having a Brillouin zone halved in z-direction. The wavefunctions should be expressed in plane-waves for both setups,

$$\psi_i^{(1)}(\mathbf{k},\mathbf{r}) = \frac{1}{\sqrt{\Omega}} \sum_{\mathbf{G}_1\in\mathcal{G}_1} C^{(1)i}_{\mathbf{k}+\mathbf{G}}\ \phi_{\mathbf{k}+\mathbf{G}_1}(\mathbf{r}), \tag{5.50}$$

$$\psi_i^{(2)}(\mathbf{k},\mathbf{r}) = \frac{1}{\sqrt{2\Omega}} \sum_{\mathbf{G}_2\in\mathcal{G}_2} C^{(2)i}_{\mathbf{k}+\mathbf{G}_2}\ \phi_{\mathbf{k}+\mathbf{G}_2}(\mathbf{r}), \tag{5.51}$$

with Ω the volume of the small unit cell, $\mathcal{G}_1$, $\mathcal{G}_2$ the two sets of G-vectors. The φ are the common plane-wave basis functions

$$\phi_{\mathbf{k}+\mathbf{G}}(\mathbf{r}) = e^{i(\mathbf{k}+\mathbf{G})\mathbf{r}}. \tag{5.52}$$

As a result of the smaller Brillouin zone the set of $\mathbf{G}$ vectors in the second setup is double as dense as in the first one, see figure 5.8. Since we cut a sphere of $|\mathbf{G}| \leq G_{max}$, the set $\mathcal{G}_2$ contains approximately double the number of vectors. So for every vector $\mathbf{G}$ out of $\mathcal{G}_1$ we assign a vector

$$\underline{\mathbf{G}} = \mathbf{G} + \tilde{K}, \quad \tilde{K} = (0, 0, \frac{\pi}{L}), \tag{5.53}$$

so that all the vectors $\{\mathbf{G}, \underline{\mathbf{G}}\}$ form the second set $\mathcal{G}_2$. This assignment works only approximately due to the shape of the sphere, but is valid for a sufficient

---

theoretical part before.

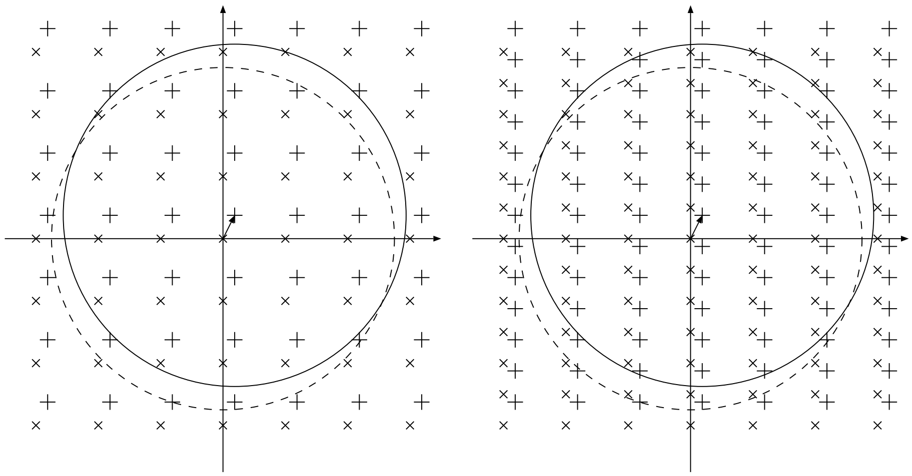

Figure 5.8: The $k_x - k_z$-plane of the reciprocal lattices for the two setups. Basis vectors are indicated by x-like crosses, $(\mathbf{k}+\mathbf{G})$-vectors for one special $\mathbf{k}$ drawn in the origin by plus-like crosses.

expansion cut-off G_{max}: Since the influence (i.e. the magnitude of the expansion coefficient) of large G-vectors vanish in the case of a valid convergence, the discrepancy can be neglected. So we can take $\mathcal{G}_2$ double as large as $\mathcal{G}_1$, and omit indices to the G-vectors since it should be clear from the context which vectors are referred to.

Let's watch the generalized eigenvalue problem (2.23). Since the plane-wave are orthogonal, the overlap has unit shape:

$$[\mathcal{H}(\mathbf{k}) - \epsilon(\mathbf{k})\mathbb{I}]\mathbf{c}(\mathbf{k}) = 0. \tag{5.54}$$

For the two setups the elements of these matrices read (see (4.3))

$$\begin{aligned} \mathcal{H}^{(1)}_{\mathbf{G},\mathbf{G}'}(\mathbf{k}) &= \frac{\hbar^2}{2m}|\mathbf{k}+\mathbf{G}|^2\delta_{\mathbf{G}\mathbf{G}'} + V^{(1)}_{(\mathbf{G}-\mathbf{G}')}, \quad V^{(1)}_{(\mathbf{G}-\mathbf{G}')} = \frac{1}{\Omega}\int\limits_{uc_1} d^3r\ e^{-i(\mathbf{G}-\mathbf{G}')\mathbf{r}}\ V_{eff}(\mathbf{r}) \\ \mathcal{H}^{(2)}_{\mathbf{G},\mathbf{G}'}(\mathbf{k}) &= \frac{\hbar^2}{2m}|\mathbf{k}+\mathbf{G}|^2\delta_{\mathbf{G}\mathbf{G}'} + V^{(2)}_{(\mathbf{G}-\mathbf{G}')}, \quad V^{(2)}_{(\mathbf{G}-\mathbf{G}')} = \frac{1}{2\Omega}\int\limits_{uc_2} d^3r\ e^{-i(\mathbf{G}-\mathbf{G}')\mathbf{r}}\ V_{eff}(\mathbf{r}), \end{aligned} \tag{5.55}$$

integrations performed over the real space units cells one (uc_1) and two (uc_2).

Now we want to relate the Hamilton matrices of the two systems. Since the function V_{eff} is periodic in the first unit cell uc_1 (thus twice periodic in uc_2), and an exponential $\exp\left(i(\mathbf{G}-\underline{\mathbf{G}}')\mathbf{r}\right)$ is simple periodic in uc_2, contributions of the potential of mixed G-vectors vanish:

$$V^{(2)}_{(\mathbf{G}-\underline{\mathbf{G}}')} = V^{(2)}_{(\underline{\mathbf{G}}-\mathbf{G}')} = 0. \tag{5.56}$$

If we therefore rearrange the vectors of $\mathcal{G}_2$ when applying them on $\mathcal{H}$ to group the vectors of $\mathcal{G}_1$ first, we obtain for the Hamiltonian the block form

$$\mathcal{H}^{(2)} = \begin{pmatrix} \mathcal{H}^{(2a)} & 0 \\ 0 & \mathcal{H}^{(2b)} \end{pmatrix}, \tag{5.57}$$

the submatrix (a) taking the contributions of the undashed, (b) taking those of the dashed G-vectors.

Contributions $(\underline{\mathbf{G}}-\underline{\mathbf{G}}')$ to the potential are identical to contributions $(\mathbf{G}-\mathbf{G}')$ of the corresponding undashed G-vectors. In the formula for the potential, the double integration range cancels with the factor $\frac{1}{2}$ in front of the integral, and the contribution is the same as in the small setup:

$$V^{(2)}_{(\underline{\mathbf{G}}-\underline{\mathbf{G}}')} = V^{(2)}_{(\mathbf{G}-\mathbf{G}')} = V^{(1)}_{(\mathbf{G}-\mathbf{G}')}. \tag{5.58}$$

Since the kinetic part of $\mathcal{H}^{(2a)}$ is identical to $\mathcal{H}^{(1)}$, so is the whole submatrix. Let's turn focus on $\mathcal{H}^{(2b)}$. It reads

$$\mathcal{H}^{(2b)}_{\underline{\mathbf{G}},\underline{\mathbf{G}}'}(\mathbf{k}) = \frac{\hbar^2}{2m}|\mathbf{k}+\underline{\mathbf{G}}|^2\delta_{\underline{\mathbf{G}}\underline{\mathbf{G}}'} + V_{(\underline{\mathbf{G}}-\underline{\mathbf{G}}')}. \tag{5.59}$$

We assume time reversal symmetry, i.e. $\mathcal{H}(\mathbf{k})$ yields the same set of eigenvectors and eigenvalues for $-\mathbf{k}$. We apply this on our submatrix $\mathcal{H}^{(2b)}$. Because of $\underline{\mathbf{G}} = \mathbf{G} + \tilde{K}$ and (5.58), our matrix elements are equivalent to

$$\begin{aligned} \mathcal{H}^{(2b)}_{\underline{\mathbf{G}},\underline{\mathbf{G}}'}(\mathbf{k}) &= \frac{\hbar^2}{2m}|(\tilde{K}-\mathbf{k})+\mathbf{G}|^2\delta_{\mathbf{G}\mathbf{G}'} + V_{(\mathbf{G}-\mathbf{G}')} && (5.60)\\ &= \mathcal{H}^{(1)}_{\mathbf{G},\mathbf{G}'}(\tilde{K}-\mathbf{k}). && (5.61) \end{aligned}$$

With defining a backfolding operator $\mathcal{T}_k : \mathbf{k} \to \tilde{K} - \mathbf{k}$, the Hamiltonian reads

$$\mathcal{H}^{(2)}(\mathbf{k}) = \begin{pmatrix} \mathcal{H}^{(1)}(\mathbf{k}) & 0 \\ 0 & \mathcal{H}^{(1)}(\mathcal{T}_k\mathbf{k}) \end{pmatrix}. \tag{5.62}$$

The spectrum of such a matrix is the sum of the spectra of the submatrices. The eigenvectors are filled up with zeros in its additional components. If the small setup has the eigenvalues and eigenvectors

$$\{\epsilon^{(1)}_j(\mathbf{k})\}, \quad \{|j\mathbf{k}\rangle\} = \left\{\left(C^{(1)j}_{(\mathbf{k}+\mathbf{G})}\right)\right\}, \tag{5.63}$$

those of the large setup are

$$\begin{aligned} \{\epsilon^{(2)}_i(\mathbf{k})\} &= \{\epsilon^{(1)}_j(\mathbf{k})\} \cup \{\epsilon^{(1)}_j(\mathcal{T}_k\mathbf{k})\} \quad \text{and} \\ \{|i\mathbf{k}\rangle\} &= \left\{\begin{pmatrix} C^{(1)j}_{(\mathbf{k}+\mathbf{G})} \\ 0 \end{pmatrix}\right\} \cup \left\{\begin{pmatrix} 0 \\ C^{(1)j}_{(\mathcal{T}_k\mathbf{k}+\mathbf{G})} \end{pmatrix}\right\} && (5.64) \end{aligned}$$

(with j (i) running over all bands of the small (large) system).

It should be noted that the derivations given above only fit approximately, due to the finite set of **G**-vectors. This is illustrated in figure 5.8, where a sample cutting sphere is plotted. For such a small set of vectors, it is barely possible to make a reasonable mapping (5.53). This effect should diminish for an increasing number of basis functions.

The experience shows that the distinction (5.64) into two different kinds of eigenvectors is also valid for the same system in an LAPW basis. This has been tested for the calculation presented in the next subsection.

However, if the backfolding involves a more complex transformation of basis vectors, these results – the form of the eigenvectors (5.64) – do not stand strictly anymore.

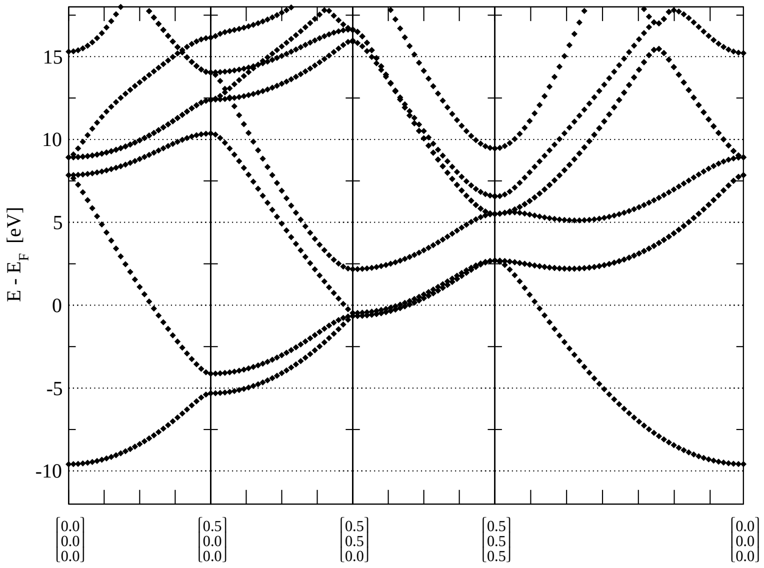

Figure 5.9: Band structure for scc Aluminum, setup 1 (small).

5.4.3 Illustration

This effect should be demonstrated now by some band structures for this system. Figures 5.9 and 5.10 show the band structures for the two systems along the path $(0,0,0) \to (\frac{1}{2},0,0) \to (\frac{1}{2},\frac{1}{2},0) \to (\frac{1}{2},\frac{1}{2},\frac{1}{2}) \to (0,0,0)$, each in internal coordinates. Due to the symmetry mentioned above, every plot $\mathbf{k}_1 \to \mathbf{k}_2$ in the large system is the sum of the plots $\mathbf{k}_1 \to \mathbf{k}_2$ and $(\tilde{K} - \mathbf{k}_1) \to (\tilde{K} - \mathbf{k}_2)$ of the small system (with $\tilde{K} = (0,0,\frac{2\pi}{L})$).

Due to the simple kind of backfolding in this setup, one sees the backfolding nicely in a plot along z-direction. In figure 5.11 the path $(\frac{1}{2},\frac{1}{2},0) \to (\frac{1}{2},\frac{1}{2},\frac{1}{2})$ is

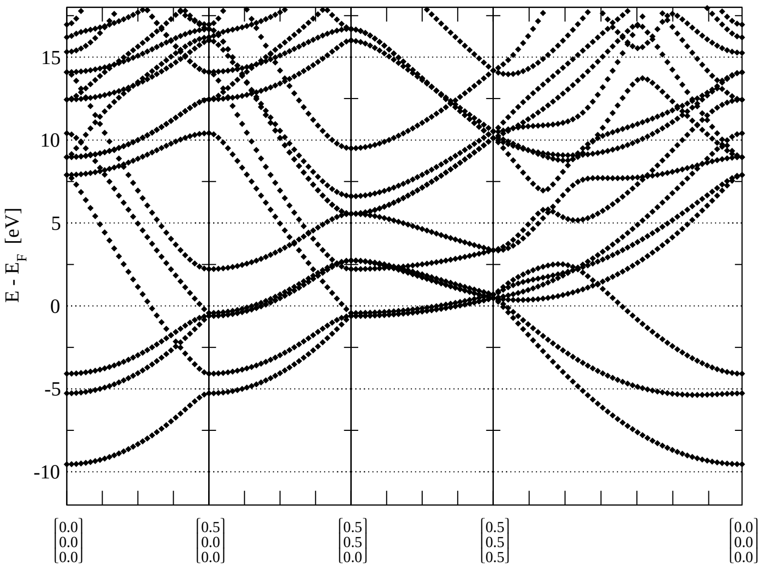

Figure 5.10: Band structure for scc Aluminum, setup 2 (large).

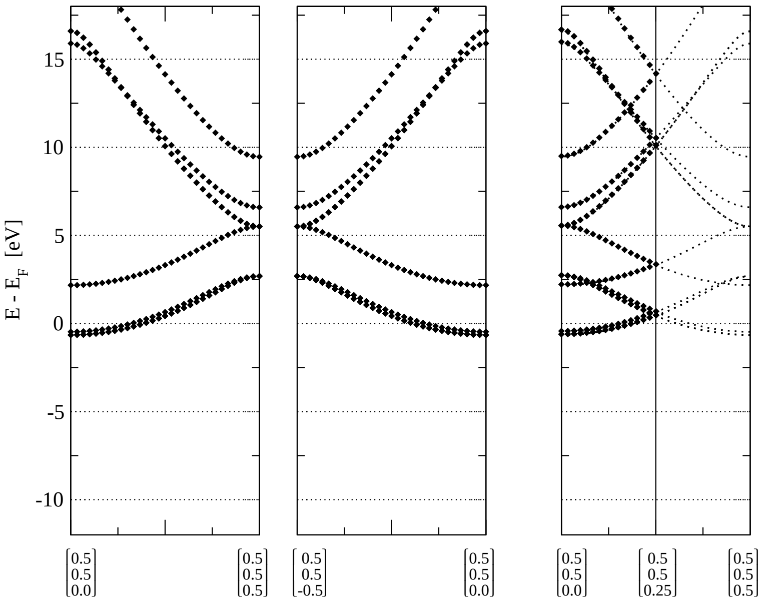

Figure 5.11: Backfolded band structure parallel to z-direction. On the left two band structures of the small system are shown that overlap to the band structure of the large system on the right.

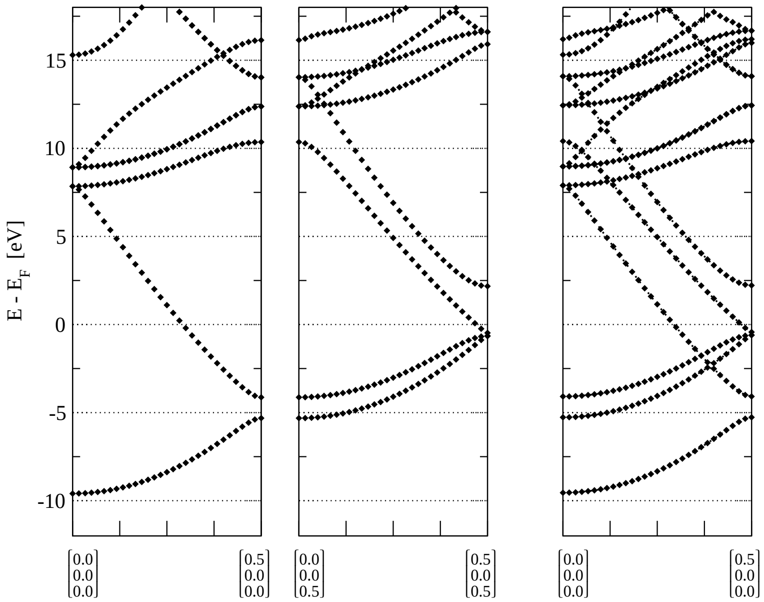

Figure 5.12: Backfolded band structure perpendicular to z-direction. The right band structure (large setup) is the sum of the two on the left (small setup).

shown, that is the third section of figure 5.10. The band structure of the large system is given by that of the small system overlapped with the additional path $(\frac{1}{2}, \frac{1}{2}, \frac{1}{2}) \to (1, \frac{1}{2}, \frac{1}{2})$.

In figure 5.12 the band structure $(0,0,0) \to (\frac{1}{2}, 0, 0)$ is plotted. The bands of the large system on the right are those of the small system along the same line on the very left, superposed by the bands $(0, 0, \frac{1}{2}) \to (\frac{1}{2}, 0, \frac{1}{2})$. Here it is already difficult to distinguish the two kinds of bands by a simple glimpse.

5.4.4 Consequences for computation

The calculation of a physical property (i.e. the expectation value of a hermitian operator) must be the same whatever choice of the unit cell has been made. Since the band structures change, one might get the impression that this rule is violated.

One essential ingredient of the dielectric function (3.39) are the transitions from one band to another, that is a double sum over occupied and unoccupied states. This summation will change if the band structure changes. The joint density of states (JDOS) for example, given by (3.42), relies on these transitions only, meaning only on the gradient of the energy differences. It does not depend additionally on matrix elements like the dielectric function (3.39). This leads to different results for a backfolded setup.

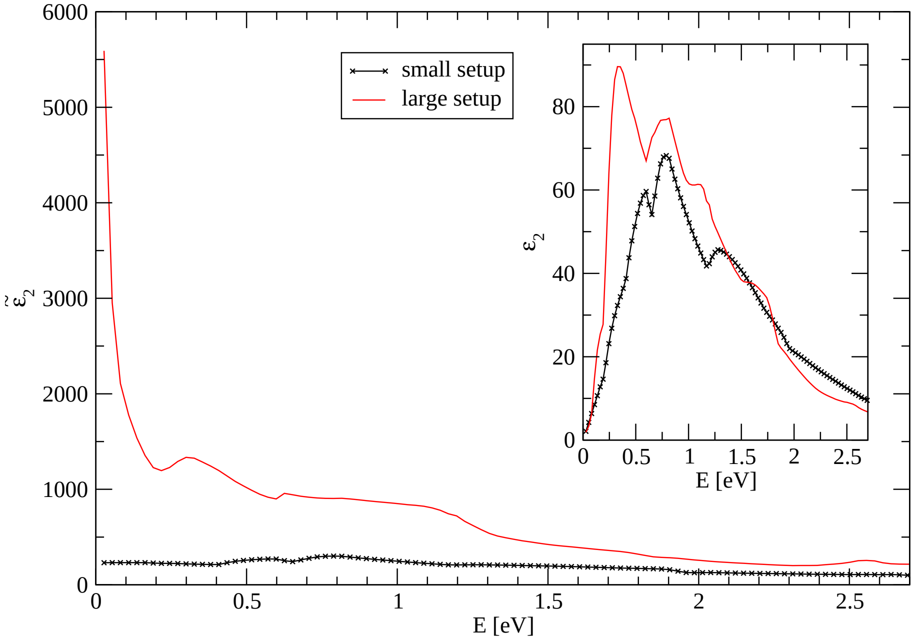

Figure 5.13: Dielectric function of scc Aluminum with (small graph, ε_2) and without (large graph, $\tilde{\varepsilon}_2$) inclusion of matrix elements (288 k-points) for small and large unit cell.

To show this, the dielectric function (3.39) is plotted in graph 5.13 with matrix elements neglected, i.e. the numerator equal to one. Though not the same quantity, this term suffers the same effect with respect to backfolding as the JDOS does. It can diverge for small energies due to the factor $\frac{1}{\omega^2}$. This difference for the two setups does not contradict physics since the JDOS is not an observable and does not have a physical meaning by itselves.

The dielectric function on the other hand yields the same results for both setups due to the momentum matrix elements included in its mathematical description. These matrix elements have the property to vanish if being applied on a regular and a backfolded eigenfunction:

$$\langle f\mathbf{k}|\nabla|\imath\mathbf{k}\rangle = 0 \quad \text{for backfolded transition,} \tag{5.65}$$

that is one state of $\imath$ or f being backfolded, the other one regular. For the simple setup of section 5.4, this can be seen easily from the form of the eigenvectors (5.64) and the form of the matrix elements in plane-wave basis (4.4).

5.5 Resulting problems in the integration

Up to now, the interesting insights of the previous section do not pose any analytical problems. But in the numerical treatment, problems appear due to the interpolation between k-points made in the integration scheme described above. The two different kinds of problems encountered in the implementation are described in this section.

Before describing the details, one should remember the way a computer handles bands. A human can connect k-points logically to bands by watching a band-structure, or can give it a mathematical character. Initially, computers can only enumerate the eigenvalues, and uses the according eigenvectors. It needs additional effort [YKS] to recognize band crossings.

5.5.1 The Influence of Degeneracy

The first problem with backfolding arises at points with degenerated energy eigenvalues. At these points the eigenvectors are determined only up to linear combinations of each other. An example for degenerated eigenvalues is sketched in figure 5.14. For instance, k_3 could be the zone boundary. It is known that the matrix elements vanish for a degenerate energy eigenvalues,

$$\langle f\mathbf{k}_g|\nabla|\imath\mathbf{k}_g\rangle = 0 \quad \text{for} \quad E_\imath(\mathbf{k}_g) = E_f(\mathbf{k}_g), \tag{5.66}$$

as in our case. (This is shown by Mavropoulos, Papanikolaou and Dederichs [MPD].) It should be valid in the limit $\mathbf{k} \to \mathbf{k}_g$, too. Therefore, one should not expect problems from this.

The situation is different if you consider transitions to another band c in a system possessing backfolding. In our figure, let bands a and c be regular, while b is backfolded. Transitions $b \to c$ should not give any contributions. This is consistent with the image that according to (5.64), the eigenvectors of bands b and c have the form

$$|ak\rangle \sim \begin{pmatrix} * \\ 0 \end{pmatrix}, \quad |bk\rangle \sim \begin{pmatrix} 0 \\ * \end{pmatrix}, \quad |ck\rangle \sim \begin{pmatrix} * \\ 0 \end{pmatrix}, \quad k \in (k_1, k_3). \tag{5.67}$$

At k_3, however, due to the intermixture of a and b, the eigenvectors take the form

$$|ak\rangle \sim \begin{pmatrix} * \\ * \end{pmatrix}, \quad |bk\rangle \sim \begin{pmatrix} * \\ * \end{pmatrix}, \tag{5.68}$$

resulting in a matrix element $M_{cb}(k_3) \neq 0$. In the analytical solution this is no problem due to the singularity of this point (or plane in three dimensions, respectively). In a linear interpolation scheme, though, this leads to finite contributions, as sketched in the small picture in figure 5.14.

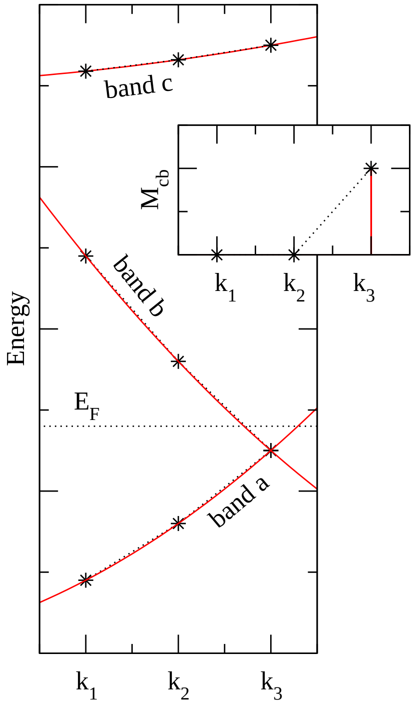

Figure 5.14: One-dimensional illustration of degeneracy. The straight red lines are the true bands, while the dotted black ones are interpolated linearly from the energy values (plotted as stars) at the mesh points k_1,k_2,k_3. The horizontal dotted line indicates the Fermi energy. In the small picture, a linear interpolation is sketched in dotted black, the true discontinuous path in solid red.

A possible solution: It is neither common nor possible without additional numerical effort to determine the "natural form" $|\imath\mathbf{k}_g\rangle_n$ of the wavefunctions at a k-point $\mathbf{k}_g$ possessing degeneracy (that would be $|\imath\mathbf{k}_g\rangle_n = \lim_{\mathbf{k}\to\mathbf{k}_g} |\imath\mathbf{k}\rangle$). Furthermore it is quite improbable (if possible at all with limited numerical precision) for a sample k-point within the Brillouin zone (excluding the origin) to hit a point of degeneracy. On the other hand degeneracy on the Brillouin zone's boundary and at high symmetry points in it (which are in turn boundaries of the irreducible part of the Brillouin zone) is very common. Experience affirms that matrix elements like $M_{cb}(k)$ quickly vanish when moving off the high symmetry (see next subsection).

Therefore a simple solution is just to shift all k-points marginally off the boundary inside the irreducible wedge. If backfolding is absent, this leads to only a marginal but noticeable error, due to the quick variations of the matrix elements close to high-symmetry planes. In the presence of backfolding, the effect is similar to neglecting the matrix elements (shown in figure 5.13): The dielectric function will get additional contributions due to wrong interpolation, especially big values for small frequencies.

5.5.2 The Influence of Band crossing

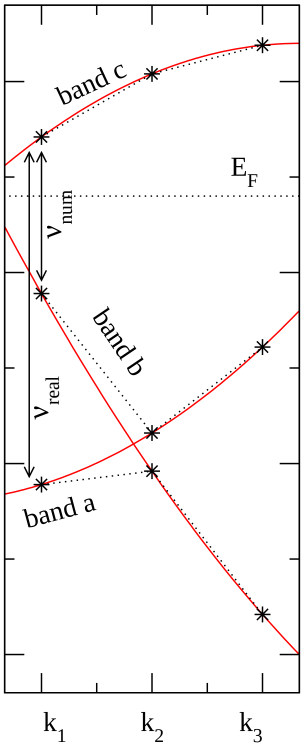

Figure 5.15: One-dimensional example for band crossing. The straight red lines are the true bands, while the dotted black lines are interpolated from the energy values (plotted as stars) at the mesh points k_1,k_2,k_3. Fermi energy is dotted in the upper third.

In the case of band crossing, the interpolation errors have a significant influence. This is illustrated for a one-dimensional example in figure 5.15. The true bands are approximated linearly from the energy values at three sampling k-points k_1,k_2,k_3. As in the sketch before the bands are labeled a,b,c. For a human observer this refers the true bands, while a computer gives these labels to the eigenvalues ordered from bottom to up.

Let the bands a and c be regular, while band b is backfolded, and focus on the interval $[k_1, k_2]$. According to (5.64) the eigenvalues at k_1 take the form

$$|ak_1\rangle \sim \begin{pmatrix} * \\ 0 \end{pmatrix}, \quad |bk_1\rangle \sim \begin{pmatrix} 0 \\ * \end{pmatrix}, \quad |ck_1\rangle \sim \begin{pmatrix} * \\ 0 \end{pmatrix}, \tag{5.69}$$

and the form

$$|ak_2\rangle \sim \begin{pmatrix} 0 \\ * \end{pmatrix}, \quad |bk_2\rangle \sim \begin{pmatrix} * \\ 0 \end{pmatrix}, \quad |ck_2\rangle \sim \begin{pmatrix} * \\ 0 \end{pmatrix} \tag{5.70}$$

at point k_2. This results in matrix elements for a transition $b \to c$ of the form

$$M_{cb}(k_1) = 0, \quad \text{but} \quad M_{cb}(k_2) \neq 0. \tag{5.71}$$

Due to the non-vanishing matrix element at k_2, the matrix element is interpolated in $[k_1, k_2]$ continuous in the range $[0, M_{cb}(k_2)]$. In the given example, this results in transitions at low frequencies ν_{num} (see figure 5.15), while analytically (and for an infinitely dense mesh) only transitions down to ν_{real} are possible in this interval.

The impact on the current calculations are strong since though also occurring in its absence, the effect is stronger with backfolding present due to the larger number of bands. Further on, the differences resulting from matrix elements equal zero being interpolated incorrectly are crucial, especially for small energies due to the factor $\frac{1}{\omega^2}$ that goes into the dielectric function (3.39).

An approach to avoid the problem: A method to minimize the contribution of backfolding to this effect is to renumber the bands. This is possible up to a certain point for crossings of regular bands with backfolded ones, as mentioned earlier (5.64).

In figure 5.16, this method has been applied to aluminum for a mesh of 288 k-points. Only with this method one restores the correct absorption edge of the curve. Calculations show that without reordering of bands, this effect is still present for a calculation involving 11000 k-points.

The higher the eigenvalues are, and the closer the k-points to high symmetry positions, the worse is classification into regular and backfolded ones. The first item is not too serious because transitions of higher energy contribute less to the dielectric function, due to the prefactor $\frac{1}{\omega^2}$. Second one can assume band crossings of regular and backfolded bands not to appear in the very close vicinity of high-symmetry planes. Starting from this one can hope to get good results with this method.

In figure 5.17 the actual decay of overlap and absolute value of matrix elements is shown. The observed system is the second test system in section 5.7, fcc Copper. The two lowest bands are examined along the k-vectors (z, z, z) for $z \in [0.499, 0.5]$. The plot is double logarithmic. It gives an idea of how far to shift k-points off the boundary so that the matrix elements vanish (as they should) and the bands can be classified correctly.

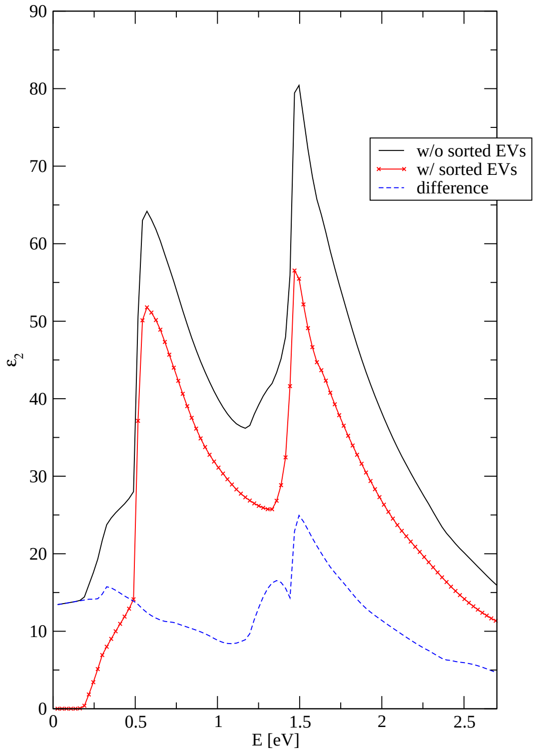

Figure 5.16: Dielectric function for fcc Aluminum, with and without sorted eigenvalues to correct crossing with backfolded bands (288 k-points).

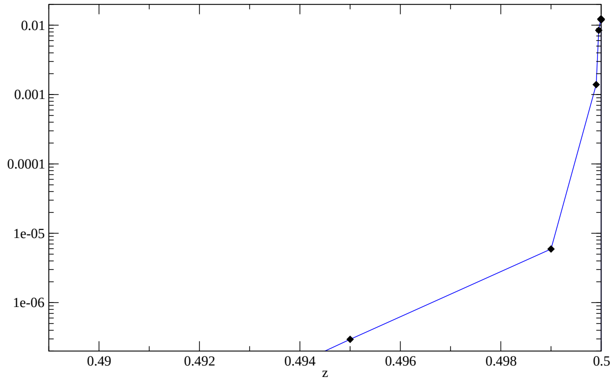

Figure 5.17: The overlap of wavefunctions 1 and 2 of an fcc Copper system.

5.6 A Note on Computational Demands

For sophisticated spectral computations you need an adequate set of k-points – possibly in the order of thousands. This meets the fact that for large systems with a big number of electrons, the number of transitions roughly scales quadratically to it. Together this can result in quite big demands of computer memory, so that one has to consider the question how to provide these matrix elements to your integration routine.

It turns out that the calculation of the matrix elements (and herein the interstitial contribution) is the major computational effort. So one can calculate the MMEs in advance, resulting in minimal computational costs and biggest memory demands. On the other hand the matrix elements can be computed on-the-fly, abandon the use of the big array memory, but needing to calculate the same matrix elements several times. In between, you can try to cache selected elements in memory to combine the advantages of both approaches with minimal drawbacks.

At this point, the special way of connections of your k-points to tetrahedra and the order of tetrahedra can be of big help. For instance, regard a typical tetrahedra set connecting nearest neighbors in a set of n_k k-points equidistant in the three spatial coordinates. This tetrahedra should be arranged in layers, e.g. in z-direction, with the same order in each layer (according to the layer shape which may differ).

If one processes the tetrahedra sequentially, the data of the corresponding k-points (including the matrix elements) are not needed only for a short time. Conversely, even if one does not want to calculate the matrix elements multiple times, you need to store only n_{sim} matrix elements at the same time, where n_{sim} can be considerably smaller than n_k.

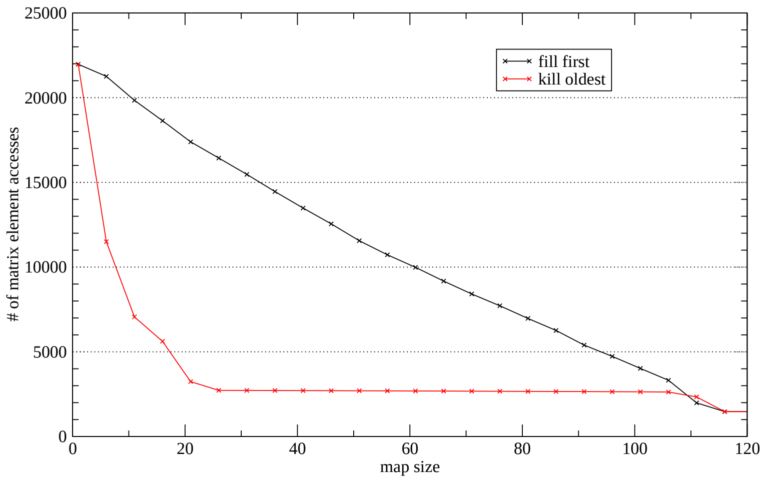

Figure 5.18: Computational amount depending on cache size (1470 k-points, 6591 tetrahedra).

If you take a cache smaller than these n_{sim} entries, you will have to calculate matrix elements partly again since you have to skip some which you need later.

But you can still take good advantage of that method, depending on which matrix elements you skip. In figure 5.18 this is illustrated for a k-point of 1470 points (it is a prism-shaped box with 14 equidistant points per edge), giving 6591 tetrahedra. Only matrix elements for $n_{sim} = 116$ k-points are needed simultaneously not to calculate them repeatedly.

If you lower the size of your cache below this value, your number of calculations increase, depending on your strategy. The point $(116, 1470)$ at the lower right is the starting point of a complete caching. If the cache is full when a matrix element should be stored, the first strategy writes the new element in the beginning of the cache, while the second one looks for the oldest element in cache. Though the number of computations quickly nearly doubles for a small decrease of cache size ($\sim (106, 2650)$), it stays below 3000 – roughly double the computational amount – for even a fifth of the starting size.

5.7 Test calculation

In this section I investigate the influence of

- backfolding
- band crossing
- Fermi energy (just remark).
- number of k-points

Remarks on computational demand, scaling
Restriction of FLEUR, larger cells, backfolding...
Run-flow diagram of my code??
MME plots

In this section two calculations are compared to literature. The parameters are listed in appendix D.

5.7.1 Aluminum

In nature, Aluminum exists in the face-centered cubic configuration. This can be modeled in the basis

$$\mathcal{A}_1 = L \begin{pmatrix} \frac{1}{2} & \frac{1}{2} & 0 \\ \frac{1}{2} & 0 & \frac{1}{2} \\ 0 & \frac{1}{2} & \frac{1}{2} \end{pmatrix}, \quad \mathcal{B}_1 = \frac{2\pi}{L} \begin{pmatrix} 1 & 1 & -1 \\ 1 & -1 & 1 \\ -1 & 1 & 1 \end{pmatrix} \tag{5.72}$$

of real and reciprocal space. In the current calculation it is modeled in the real-space and reciprocal-space basis

$$\mathcal{A}_2 = L \begin{pmatrix} \frac{1}{2} & \frac{1}{2} & 0 \\ \frac{1}{2} & -\frac{1}{2} & 0 \\ 0 & 0 & 1 \end{pmatrix} , \quad \mathcal{B}_2 = \frac{2\pi}{L} \begin{pmatrix} 1 & 1 & 0 \\ 1 & -1 & 0 \\ 0 & 0 & 1 \end{pmatrix} , \tag{5.73}$$

with two atoms per unit cell on internal coordinates $(0,0,0)$ and $\frac{1}{2}(1,1,1)$. The used lattice parameter $L_{num} = XXXa_0$ was converged to the minimum of the total energy. A bandstructure (along the same path as those in section **??**) is shown in figure 5.19, together with the density of states. The $3s$ electrons of this system show a behaviour similar to free electrons, as can be seen in the parabola-like bands in the bandstructure, and in the DOS close to $\sqrt{E}$. On can compare these results to those of the simple-cubic systems in section 5.4.

Figure 5.19: The bandstructure $(0,0,0) \rightarrow (\frac{1}{2},0,0) \rightarrow (\frac{1}{2},\frac{1}{2},0) \rightarrow (\frac{1}{2},\frac{1}{2},\frac{1}{2}) \rightarrow (0,0,0)$ of Aluminum in fcc coordination is shown on the left. The right plot contains the according Density of states.

The (imaginary) dielectric function has already been shown in figure 5.16 for a small number of k-points to demonstrate the influence of the sorting of eigenvalues. In figure 5.20 it is shown for different larger number of k-points. It shows the slow convergence known from literature. Furthermore, two characteristic peaks are located at 0.5eV and 1.6eV.

This aggrees with literature.

Numerical considerations: The convergence has been done for 6 k-points and alternatively for 100 k-points. The dielectric function does not show a visible difference.

Figure 5.20: Imaginary dielectric function for fcc Aluminum for different sets of k-points.

Figure 5.21: The imaginary part of the dielectric function for fcc Aluminum for two different lattice constants L_{exp}, $L_{num} = XXX L_{exp}$.

As a second test, in figure 5.21 the dielectric function was calculated for the experimental lattice constant $L_{exp} = 4.04\mathring{A} = 7.64 a_0$, a_0 being the Bohr radius (see appendix C), i.e. a difference of XXX percent. It can be seen that XXX.

5.7.2 Copper

The second test system is copper, which condensates in the face-centered cubic structure as well, therefore the same unit cell is used. In figure 5.17 the overlap for two bands of this system has been shown. Bandstructure and DOS are shown in figure 5.22. The converged lattice parameter is $L_{num} = XXX\mathring{A}$.

The dielectric function is shown in 5.23. Literature XXX.

Figure 5.22: Bandstructure and Density of states of Copper.

Figure 5.23: Imaginary part of the dielectric function of Copper.

Chapter 6

Results

Blabla

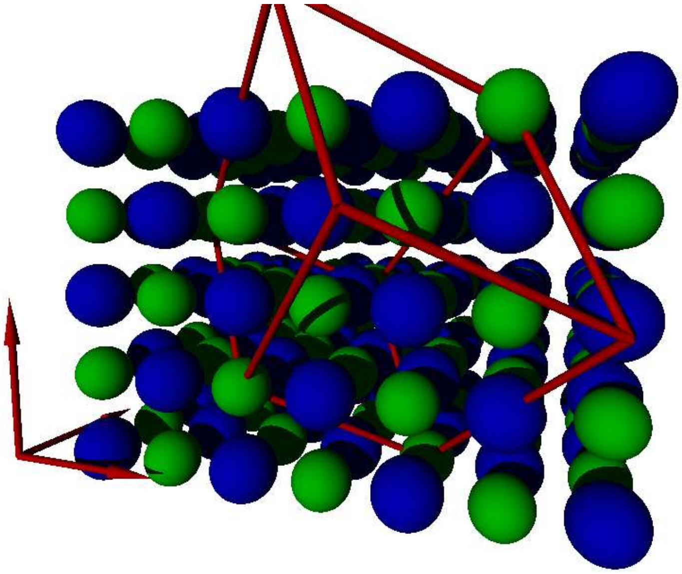

Figure 6.1: GeTe fcc structure.

6.1 GeTe compounds

Calculate GeTe in zincblende structure. Between zincblende and amorphous, no big difference in refraction is experienced, but between amorphous and rocksalt.

- GeTe cubic, trigonal
- Ge1Sb2Te4?

Show:

- Description of materials
- Lattice constants, Birge fit!
- DOS,Bandstructures
- charge density plots?
- Optical properties
- Experiments
- Comparison to measurements

6.2 Calcopyrites

- AgInTe2
- AgSbTe2
- AuInTe2
- AuSbTe2
- AuSnTe2

Chapter 7

Conclusion

Appendix A

Momentum matrix elements

The matrix elements of the momentum operator should be expressed in terms of the LAPW basis set in summed form (4.21), i.e.

$$\psi_\imath(\mathbf{k},\mathbf{r}) = \begin{cases} \dfrac{1}{\sqrt{\Omega}} \displaystyle\sum_{\mathbf{G}} C^{\imath}_{\mathbf{k}+\mathbf{G}} e^{i(\mathbf{k}+\mathbf{G})\mathbf{r}} & \mathbf{r} \in \mathrm{IS} \\ \displaystyle\sum_{l=0}^{l_{max}} \sum_{m=-l}^{l} [A^{\imath,\alpha}_{lm}(\mathbf{k}) u_l(r;E_l) + & \\ \qquad\qquad B^{\imath,\alpha}_{lm}(\mathbf{k}) \dot{u}_l(r;E_l)]\, Y_{lm}(\hat{\mathbf{r}}) & \mathbf{r} \in \mathrm{MT}_\alpha. \end{cases} \tag{A.1}$$

The interstitial part of this matrix element is derived in section 5.1.1. The part inside the muffin-tins is more lengthy to derive and therefore done here. The matrix element is not calculated in the carthesian basis but in the natural basis $(\partial_x + i\partial_y, \partial_x - i\partial_y, \partial_z)$. In spherical coordinates these partial derivatives read

$$\begin{aligned} \partial_x \pm i\partial_y &= \sin\theta e^{\pm i\varphi} \tfrac{\partial}{\partial r} + \tfrac{1}{r} e^{\pm i\varphi} \left(\cos\theta \tfrac{\partial}{\partial\theta} \pm \tfrac{i}{\sin\theta} \tfrac{\partial}{\partial\varphi} \right) \\ \partial_z &= \cos\theta \tfrac{\partial}{\partial r} - \tfrac{1}{r\sin\theta} \tfrac{\partial}{\partial\theta}. \end{aligned} \tag{A.2}$$

The radial and spherical derivatives separate. Introducting the abbreviations

$$\begin{aligned} F^{(1)}_{lm} &= -\sqrt{\tfrac{(l+m+1)(l+m+2)}{(2l+1)(2l+3)}} \\ F^{(2)}_{lm} &= \sqrt{\tfrac{(l-m)(l-m-1)}{(2l-1)(2l+1)}} \\ F^{(3)}_{lm} &= \sqrt{\tfrac{(l-m+1)(l-m+2)}{(2l+1)(2l+3)}} \\ F^{(4)}_{lm} &= -\sqrt{\tfrac{(l+m)(l+m-1)}{(2l-1)(2l+1)}} \\ F^{(5)}_{lm} &= \sqrt{\tfrac{(l-m+1)(l+m+1)}{(2l+1)(2l+3)}} \\ F^{(6)}_{lm} &= \sqrt{\tfrac{(l-m)(l+m)}{(2l-1)(2l+1)}}, \end{aligned} \tag{A.3}$$

the recurrence relations of the Legendre polynomials yield the equations

$$\begin{aligned} e^{+i\varphi}\sin\theta Y_{l,m} &= F^{(1)}_{lm}Y_{l+1,m+1} &+& \; F^{(2)}_{l,m}Y_{l-1,m+1} \\ e^{+i\varphi}\sin\theta Y_{l,m} &= F^{(3)}_{lm}Y_{l+1,m-1} &+& \; F^{(4)}_{l,m}Y_{l-1,m-1} \; . \\ \cos\theta Y_{l,m} &= F^{(5)}_{lm}Y_{l+1,m} &+& \; F^{(6)}_{lm}Y_{l-1,m} \end{aligned} \tag{A.4}$$

Furthermore the relations

$$\begin{aligned} e^{+i\varphi}\left(\cos\theta\frac{\partial}{\partial\theta}+\frac{i}{\sin\theta}\frac{\partial}{\partial\varphi}\right)Y_{lm} &= -lF^{(1)}_{lm}Y_{l+1,m+1} &+& \; (l+1)F^{(2)}_{lm}Y_{l-1,m+1} \\ e^{-i\varphi}\left(\cos\theta\frac{\partial}{\partial\theta}-\frac{i}{\sin\theta}\frac{\partial}{\partial\varphi}\right)Y_{lm} &= -lF^{(3)}_{lm}Y_{l+1,m-1} &+& \; (l+1)F^{(4)}_{lm}Y_{l-1,m-1} \\ -\sin\theta\frac{\partial}{\partial\theta}Y_{lm} &= -lF^{(5)}_{lm}Y_{l+1,m} &+& \; (l+1)F^{(6)}_{lm}Y_{l-1,m} \end{aligned} \tag{A.5}$$

In order to apply the derivatives on the LAPW functions, we define the functions (ommiting the muffin-tin index α for convenience)

$$\begin{aligned} U^i_{lm} &= \; A^{i,\alpha}_{lm}(\mathbf{k})u_l(r;E_l)+B^{i,\alpha}_{lm}(\mathbf{k})\dot{u}_l(r;E_l) \\ V^i_{lm} &= \frac{\partial}{\partial r}\; U^i_{lm} \\ &= \; A^{i,\alpha}_{lm}(\mathbf{k})u'_l(r;E_l)+B^{i,\alpha}_{lm}(\mathbf{k})\dot{u}'_l(r;E_l) \\ W^i_{lm} &= \frac{1}{r}\cdot\; U^i_{lm} \\ &= \frac{1}{r}\cdot\; \left(A^{i,\alpha}_{lm}(\mathbf{k})u_l(r;E_l)+B^{i,\alpha}_{lm}(\mathbf{k})\dot{u}_l(r;E_l)\right) \end{aligned} \tag{A.6}$$

First component $\partial_x + i\partial_y$: If one expresses the LAPWs with these functions (A.6) utilizing the relations (A.2) and (A.5), one yields for the operation of the operator

$$\begin{aligned} (\partial_x+i\partial_y)\psi_i(\mathbf{k},\mathbf{r}) &= \sum_{lm}\Big[(V^i_{lm}-l\;W^i_{lm})F^{(1)}_{lm}Y_{l+1,m+1} \\ &\qquad (V^i_{lm}-(l+1)W^i_{lm})F^{(2)}_{lm}Y_{l-1,m+1}\Big]\,, \end{aligned} \tag{A.7}$$

omitting spatial coordinates, and the summation indices running through $l = 0,\ldots,l_{max},\; m=-l\ldots l$. Multiplying the corresponding bra gives

$$\begin{aligned} &\int\limits_{MT_\alpha} d^3r\;\psi^*_f(\mathbf{k},\mathbf{r})(\partial_x+i\partial_y)\psi_i(\mathbf{k},\mathbf{r}) \\ =& \sum_{lm,l'm'}\int\limits_0^{R_\alpha} r^2dr\oint d\Omega\; U^{f*}_{l'm'}Y^*_{l'm'}\Big[(V^i_{lm}-l\;W^i_{lm})F^{(1)}_{lm}Y_{l+1,m+1}+ \\ &\qquad\qquad (V^i_{lm}-(l+1)W^i_{lm})F^{(2)}_{lm}Y_{l-1,m+1}\Big] \\ =& \sum_{lm,l'm'}\int\limits_0^{R_\alpha} r^2dr\;{}^{(1)}D1^{l'm'}_{lm}\oint d\Omega\;Y^*_{l'm'}Y_{l+1,m+1}+ \\ & \sum_{lm,l'm'}\int\limits_0^{R_\alpha} r^2dr\;{}^{(2)}D2^{l'm'}_{lm}\oint d\Omega\;Y^*_{l'm'}Y_{l-1,m+1} \end{aligned} \tag{A.8}$$

with the abbreviations for $D1$,$D2$ equal to

$$\begin{array}{rcl} {}^{(j)}D1_{lm}^{l'm'} & = & F_{lm}^{(2j-1)}U_{l'm'}^{f*}(V_{lm}^{i} - l\ W_{lm}^{i}) \\ {}^{(j)}D2_{lm}^{l'm'} & = & F_{lm}^{(2j)}U_{l'm'}^{f*}(V_{lm}^{i} - (l+1)W_{lm}^{i}). \end{array} \tag{A.9}$$

With the spherical harmonics being orthogonal,

$$\begin{array}{rcl} \oint d\Omega\ Y_{l'm'}^{*}Y_{l+1,m+1} & = & \delta_{l',l+1}\delta_{m',m+1}, \\ \oint d\Omega\ Y_{l'm'}^{*}Y_{l-1,m+1} & = & \delta_{l',l-1}\delta_{m',m+1}, \end{array} \tag{A.10}$$

the quadruple summation in the two terms reduces to each a double one:

$$\begin{array}{rcl} \sum\limits_{lm,l'm'} .{}^{(j)}D1_{lm}^{l'm'}\delta_{l',l+1}\delta_{m',m+1} & = & \sum\limits_{l=0}^{l_{max}-1}\ \sum\limits_{m=-l}^{+l} .{}^{(j)}D1_{lm}^{l+1,m+1} \\ \sum\limits_{lm,l'm'} .{}^{(j)}D2_{lm}^{l'm'}\delta_{l',l-1}\delta_{m',m+1} & = & \sum\limits_{l=0}^{l_{max}-1}\ \sum\limits_{m=-l}^{+l} .{}^{(j)}D2_{l+1,m-1}^{lm}. \end{array} \tag{A.11}$$

Please note the maximum l decreased by one. Now applying the remaining radial integration, and expanding the symbols $D1$ and $D2$ finally gives:

$$\langle f\mathbf{k}|\partial_x + i\partial_y|i\mathbf{k}\rangle = \sum_{l=0}^{l_{max}-1}\ \sum_{m=-l}^{l}$$

$$\begin{array}{cllcrlll} & [\,(& \int u_{l+1}u_l'\ r^2dr & - & l & \int u_{l+1}u_l\ rdr) & A_{l+1,m+1}^{*f}A_{l,m}^{i} & \\ + & (& \int u_{l+1}\dot{u}_l'\ r^2dr & - & l & \int u_{l+1}\dot{u}_l\ rdr) & A_{l+1,m+1}^{*f}B_{l,m}^{i} & \\ + & (& \int \dot{u}_{l+1}u_l'\ r^2dr & - & l & \int \dot{u}_{l+1}u_l\ rdr) & B_{l+1,m+1}^{*f}A_{l,m}^{i} & \\ + & (& \int \dot{u}_{l+1}\dot{u}_l'\ r^2dr & - & l & \int \dot{u}_{l+1}\dot{u}_l\ rdr) & B_{l+1,m+1}^{*f}B_{l,m}^{i}\ ] & F_{l,m}^{(1)} \\ + & [\,(& \int u_l u_{l+1}'\ r^2dr & + & (l+2) & \int u_{l+1}u_l\ rdr) & A_{l,m}^{*f}A_{l+1,m-1}^{i} & \\ + & (& \int u_l\dot{u}_{l+1}'\ r^2dr & + & (l+2) & \int u_{l+1}\dot{u}_l\ rdr) & A_{l,m}^{*f}B_{l+1,m-1}^{i} & \\ + & (& \int \dot{u}_l u_{l+1}'\ r^2dr & + & (l+2) & \int \dot{u}_{l+1}u_l\ rdr) & B_{l,m}^{*f}A_{l+1,m-1}^{i} & \\ + & (& \int \dot{u}_l\dot{u}_{l+1}'\ r^2dr & + & (l+2) & \int \dot{u}_{l+1}\dot{u}_l\ rdr) & B_{l,m}^{*f}B_{l+1,m-1}^{i}\ ] & F_{l+1,m-1}^{(2)} \end{array}$$

Second component $\partial_x - i\partial_y$: The procedure is analogous for the next component. Again (A.2) and (A.5) help to express it as

$$\begin{array}{rcl} (\partial_x - i\partial_y)\psi_i(\mathbf{k},\mathbf{r}) & = & \sum\limits_{lm}\Big[(V_{lm}^{i} - l\ W_{lm}^{i})F_{lm}^{(3)}Y_{l+1,m-1} \\ & & \qquad (V_{lm}^{i} - (l+1)W_{lm}^{i})F_{lm}^{(4)}Y_{l-1,m-1}\Big]. \end{array} \tag{A.12}$$

Multiplying the bra,

$$\begin{array}{rl} & \int\limits_{MT_\alpha} d^3r\ \psi_f^{*}(\mathbf{k},\mathbf{r})(\partial_x - i\partial_y)\psi_i(\mathbf{k},\mathbf{r}) \\ = & \sum\limits_{lm,l'm'}\int\limits_{0}^{R_\alpha} r^2dr\ {}^{(3)}D1_{lm}^{l'm'}\oint d\Omega\ Y_{l'm'}^{*}Y_{l+1,m-1} + \\ & \sum\limits_{lm,l'm'}\int\limits_{0}^{R_\alpha} r^2dr\ {}^{(4)}D2_{lm}^{l'm'}\oint d\Omega\ Y_{l'm'}^{*}Y_{l-1,m-1}, \end{array} \tag{A.13}$$

calculating the integral over the spherical harmonics and reducing the resulting fourfold summation analougous to the first component,

$$\begin{aligned}\sum_{lm,l'm'} .^{(j)}D1^{l'm'}_{lm}\delta_{l',l+1}\delta_{m',m-1} &= \sum_{l=0}^{l_{max}-1}\sum_{m=-l}^{+l} .^{(j)}D1^{l+1,m-1}_{lm} \\ = \sum_{lm,l'm'} .^{(j)}D2^{l'm'}_{lm}\delta_{l',l-1}\delta_{m',m-1} &= \sum_{l=0}^{l_{max}-1}\sum_{m=-l}^{+l} .^{(j)}D2^{lm}_{l+1,m+1},\end{aligned} \tag{A.14}$$

yields

$$\begin{aligned}\langle f\mathbf{k}|\partial_x - i\partial_y|i\mathbf{k}\rangle = \sum_{l=0}^{l_{max}-1}\sum_{m=-l}^{l} \\ [\,(\int u_{l+1}u'_l\, r^2dr &- l \int u_{l+1}u_l\, rdr)\; A^{*f}_{l+1,m-1}A^i_{l,m} \\ +\; (\int u_{l+1}\dot{u}'_l\, r^2dr &- l \int u_{l+1}\dot{u}_l\, rdr)\; A^{*f}_{l+1,m-1}B^i_{l,m} \\ +\; (\int \dot{u}_{l+1}u'_l\, r^2dr &- l \int \dot{u}_{l+1}u_l\, rdr)\; B^{*f}_{l+1,m-1}A^i_{l,m} \\ +\; (\int \dot{u}_{l+1}\dot{u}'_l\, r^2dr &- l \int \dot{u}_{l+1}\dot{u}_l\, rdr)\; B^{*f}_{l+1,m-1}B^i_{l,m}\,]\;\; F^{(3)}_{l,m} \\ +\; [\,(\int u_l u'_{l+1}\, r^2dr &+ (l+2) \int u_{l+1}u_l\, rdr)\; A^{*f}_{l,m}A^i_{l+1,m+1} \\ +\; (\int u_l\dot{u}'_{l+1}\, r^2dr &+ (l+2) \int u_{l+1}\dot{u}_l\, rdr)\; A^{*f}_{l,m}B^i_{l+1,m+1} \\ +\; (\int \dot{u}_l u'_{l+1}\, r^2dr &+ (l+2) \int \dot{u}_{l+1}u_l\, rdr)\; B^{*f}_{l,m}A^i_{l+1,m+1} \\ +\; (\int \dot{u}_l\dot{u}'_{l+1}\, r^2dr &+ (l+2) \int \dot{u}_{l+1}\dot{u}_l\, rdr)\; B^{*f}_{l,m}B^i_{l+1,m+1}\,]\;\; F^{(4)}_{l+1,m-1}.\end{aligned}$$

Third component ∂_z: The same goes for the third component:

$$\begin{aligned}\partial_z\psi_i(\mathbf{k},\mathbf{r}) &= \sum_{lm}\Big[(V^i_{lm} - l\, W^i_{lm})F^{(5)}_{lm}Y_{l+1,m} \\ &\qquad (V^i_{lm} - (l+1)W^i_{lm})F^{(6)}_{lm}Y_{l-1,m}\Big].\end{aligned} \tag{A.15}$$

Multiplication of the corresponding bra from the left:

$$\begin{aligned}&\int_{MT_\alpha} d^3r\ \psi^*_f(\mathbf{k},\mathbf{r})\partial_z\psi_i(\mathbf{k},\mathbf{r}) \\ &= \sum_{lm,l'm'}\int_0^{R_\alpha} r^2dr\ ^{(5)}D1^{l'm'}_{lm}\oint d\Omega\ Y^*_{l'm'}Y_{l+1,m} + \\ &\quad \sum_{lm,l'm'}\int_0^{R_\alpha} r^2dr\ ^{(6)}D2^{l'm'}_{lm}\oint d\Omega\ Y^*_{l'm'}Y_{l-1,m}\end{aligned} \tag{A.16}$$

Reduction of fourfold summation:

$$\begin{aligned}\sum_{lm,l'm'} .^{(j)}D1^{l'm'}_{lm}\delta_{l',l+1}\delta_{m',m} &= \sum_{l=0}^{l_{max}-1}\sum_{m=-l}^{+l} .^{(j)}D1^{l+1,m}_{lm} \\ = \sum_{lm,l'm'} .^{(j)}D2^{l'm'}_{lm}\delta_{l',l-1}\delta_{m',m} &= \sum_{l=0}^{l_{max}-1}\sum_{m=-l}^{+l} .^{(j)}D2^{lm}_{l+1,m}\end{aligned} \tag{A.17}$$

Result:

$$\langle f\mathbf{k}|\partial_z|i\mathbf{k}\rangle = \sum_{l=0}^{l_{max}-1}\sum_{m=-l}^{l}$$

$$\begin{array}{lllllll}
 & [\,(& \int u_{l+1}u_l'\; r^2dr & - & l & \int u_{l+1}u_l\; rdr) & A^{*f}_{l+1,m}A^{i}_{l,m} \\
+ & \;\;(& \int u_{l+1}\dot{u}_l'\; r^2dr & - & l & \int u_{l+1}\dot{u}_l\; rdr) & A^{*f}_{l+1,m}B^{i}_{l,m} \\
+ & \;\;(& \int \dot{u}_{l+1}u_l'\; r^2dr & - & l & \int \dot{u}_{l+1}u_l\; rdr) & B^{*f}_{l+1,m}A^{i}_{l,m} \\
+ & \;\;(& \int \dot{u}_{l+1}\dot{u}_l'\; r^2dr & - & l & \int \dot{u}_{l+1}\dot{u}_l\; rdr) & B^{*f}_{l+1,m}B^{i}_{l,m}\;] \quad F^{(5)}_{l,m} \\
+ & [\,(& \int u_l u_{l+1}'\; r^2dr & + & (l+2) & \int u_{l+1}u_l\; rdr) & A^{*f}_{l,m}A^{i}_{l+1,m} \\
+ & \;\;(& \int u_l\dot{u}_{l+1}'\; r^2dr & + & (l+2) & \int u_{l+1}\dot{u}_l\; rdr) & A^{*f}_{l,m}B^{i}_{l+1,m} \\
+ & \;\;(& \int \dot{u}_l u_{l+1}'\; r^2dr & + & (l+2) & \int \dot{u}_{l+1}u_l\; rdr) & B^{*f}_{l,m}A^{i}_{l+1,m} \\
+ & \;\;(& \int \dot{u}_l\dot{u}_{l+1}'\; r^2dr & + & (l+2) & \int \dot{u}_{l+1}\dot{u}_l\; rdr) & B^{*f}_{l,m}B^{i}_{l+1,m}\;] \quad F^{(6)}_{l+1,m-1}.
\end{array}$$

More general notation: The results for the three components can be written in the form

$$\langle f\mathbf{k}|\partial_n|i\mathbf{k}\rangle = \sum_{l=0}^{l_{max}-1}\sum_{m=-l}^{l}$$

$$\begin{array}{lllllll}
 & [\,(& \int u_{l+1}u_l'\; r^2dr & - & l & \int u_{l+1}u_l\; rdr) & A^{*f}_{l+1,m'}A^{i}_{l,m} \\
+ & \;\;(& \int u_{l+1}\dot{u}_l'\; r^2dr & - & l & \int u_{l+1}\dot{u}_l\; rdr) & A^{*f}_{l+1,m'}B^{i}_{l,m} \\
+ & \;\;(& \int \dot{u}_{l+1}u_l'\; r^2dr & - & l & \int \dot{u}_{l+1}u_l\; rdr) & B^{*f}_{l+1,m'}A^{i}_{l,m} \\
+ & \;\;(& \int \dot{u}_{l+1}\dot{u}_l'\; r^2dr & - & l & \int \dot{u}_{l+1}\dot{u}_l\; rdr) & B^{*f}_{l+1,m'}B^{i}_{l,m}\;] \quad F^{(2n-1)}_{l,m} \\
+ & [\,(& \int u_l u_{l+1}'\; r^2dr & + & (l+2) & \int u_{l+1}u_l\; rdr) & A^{*f}_{l,m}A^{i}_{l+1,m''} \\
+ & \;\;(& \int u_l\dot{u}_{l+1}'\; r^2dr & + & (l+2) & \int u_{l+1}\dot{u}_l\; rdr) & A^{*f}_{l,m}B^{i}_{l+1,m''} \\
+ & \;\;(& \int \dot{u}_l u_{l+1}'\; r^2dr & + & (l+2) & \int \dot{u}_{l+1}u_l\; rdr) & B^{*f}_{l,m}A^{i}_{l+1,m''} \\
+ & \;\;(& \int \dot{u}_l\dot{u}_{l+1}'\; r^2dr & + & (l+2) & \int \dot{u}_{l+1}\dot{u}_l\; rdr) & B^{*f}_{l,m}B^{i}_{l+1,m''}\;] \quad F^{(2n)}_{l+1,m''}
\end{array}$$

for $n = 1, 2, 3$, and ∂, m',m'' given by

$$\partial = \begin{pmatrix} \partial_x + i\partial_y \\ \partial_x - i\partial_y \\ \partial_z \end{pmatrix}, \quad m' = \begin{pmatrix} m+1 \\ m-1 \\ m \end{pmatrix}, \quad m'' = \begin{pmatrix} m-1 \\ m+1 \\ m \end{pmatrix} \quad \text{for} \quad n = \begin{pmatrix} 1 \\ 2 \\ 3 \end{pmatrix}.$$

Local orbital contribution:

Appendix B

Tetrahedron method

As already mentioned in section 5.2, Blöchl, Jepsen and Andersen [BJA94] gave a convernient general notation for the tetrahedron method. They consider integrals over the Brillouin zone (BZ) in k-space like those of the expectation value of an operator X,

$$\langle X \rangle = \frac{1}{V_G} \sum_n \int_{BZ} d^3k \; X_n(\mathbf{k}) f(\epsilon_n(\mathbf{k})), \tag{B.1}$$

where f is the fermi factor to an energy ϵ_n. V_G is the volume of the Brillouin zone, and the used k-dependent expectation value reads

$$X_n(\mathbf{k}) = \langle n\mathbf{k}|X|n\mathbf{k}\rangle. \tag{B.2}$$

They show that in tetrahedron method this integral can be written as

$$\langle X \rangle = \sum_{j,n} X_n(\mathbf{k}_j) w_{nj}. \tag{B.3}$$

This sum runs over all bands n and k-points j.

B.1 Integration weights

The weight of one k-point w_{nj} is the sum of weights it gets in each tetrahedra it belongs to. In each tetrahedra, the indices are assigned so that the energies are ordered, $\epsilon_1 < \epsilon_2 < \epsilon_3 < \epsilon_4$.

1. $\epsilon_F < \epsilon_1$

$$w_1 = w_2 = w_3 = w_4 = 0. \tag{B.4}$$

2. $\epsilon_1 < \epsilon_F < \epsilon_2$

$$\begin{aligned} w_1 &= C\left[4-(\epsilon_F-\epsilon_1)\left(\frac{1}{\epsilon_{21}}+\frac{1}{\epsilon_{31}}+\frac{1}{\epsilon_{41}}\right)\right] \\ w_2 &= C\frac{\epsilon_F-\epsilon_1}{\epsilon_{21}} \\ w_3 &= C\frac{\epsilon_F-\epsilon_1}{\epsilon_{31}} \\ w_4 &= C\frac{\epsilon_F-\epsilon_1}{\epsilon_{41}} \end{aligned} \tag{B.5}$$

with

$$C=\frac{V_T}{4V_G}\frac{(\epsilon_F-\epsilon_1)^3}{\epsilon_{21}\epsilon_{31}\epsilon_{41}}. \tag{B.6}$$

3. $\epsilon_2 < \epsilon_F < \epsilon_3$

$$\begin{aligned} w_1 &= C_1+(C_1+C_2)\frac{\epsilon_3-\epsilon_F}{\epsilon_{31}}+(C_1+C_2+C_3)\frac{\epsilon_4-\epsilon_F}{\epsilon_{41}} \\ w_2 &= C_1+C_2+C_3+(C_2+C_3)\frac{\epsilon_3-\epsilon_F}{\epsilon_{32}}+C_3\frac{\epsilon_4-\epsilon_F}{\epsilon_{42}} \\ w_3 &= (C_1+C_2)\frac{\epsilon_F-\epsilon_1}{\epsilon_{31}}+(C_2+C_3)\frac{\epsilon_F-\epsilon_2}{\epsilon_{32}} \\ w_4 &= (C_1+C_2+C_3)\frac{\epsilon_F-\epsilon_1}{\epsilon_{41}}+C_3\frac{\epsilon_F-\epsilon_2}{\epsilon_{42}} \end{aligned} \tag{B.7}$$

with

$$\begin{aligned} C_1 &= \frac{V_T}{4V_G}\frac{\epsilon_F-\epsilon_1)^2}{\epsilon_{41}\epsilon_{31}} \\ C_2 &= \frac{V_T}{4V_G}\frac{(\epsilon_F-\epsilon_1)(\epsilon_F-\epsilon_2)(\epsilon_3-\epsilon_F)}{\epsilon_{41}\epsilon_{32}\epsilon_{31}} \\ C_3 &= \frac{V_T}{4V_G}\frac{(\epsilon_F-\epsilon_2)^2(\epsilon_4-\epsilon_F)}{\epsilon_{42}\epsilon_{32}\epsilon_{41}}. \end{aligned} \tag{B.8}$$

4. $\epsilon_3 < \epsilon_F < \epsilon_4$

$$\begin{aligned} w_1 &= C\frac{\epsilon_4-\epsilon_F}{\epsilon_{41}} \\ w_2 &= C\frac{\epsilon_4-\epsilon_F}{\epsilon_{42}} \\ w_3 &= C\frac{\epsilon_4-\epsilon_F}{\epsilon_{43}} \\ w_4 &= \frac{V_T}{4V_G}-C\left[4-(\epsilon_F-\epsilon_1)\left(\frac{1}{\epsilon_{21}}+\frac{1}{\epsilon_{31}}+\frac{1}{\epsilon_{41}}\right)\right] \end{aligned} \tag{B.9}$$

with

$$C = \frac{V_T}{4V_G}\frac{(\epsilon_4 - \epsilon_F)^3}{\epsilon_{41}\epsilon_{42}\epsilon_{43}}. \tag{B.10}$$

5. $\epsilon_4 < \epsilon_F$

$$w_1 = w_2 = w_3 = w_4 = \frac{V_T}{4V_G}. \tag{B.11}$$

B.2 Number and density of states

When neglecting the matrix elements, one yields the well-known terms for the number of states $n_T(E)$ and the density of states $D_T(E)$ of one tetrahedron, which are equivalent to the formulae given for instance by Lehmann and Taut [LT72].

Neglecting the matrix elements means setting them to one, i.e. $X_n(\mathbf{k}_j) = 1$ in (B.3). With this the number of states and density of states take the form

$$n_T(\epsilon) = \sum_{i=1}^{4} w_i, \quad D_T(\epsilon) = \frac{\partial}{\partial\epsilon} n_T(\epsilon), \tag{B.12}$$

and take the following values in the five regions:

1. $\epsilon_F < \epsilon_1$

$$\begin{aligned} n_T(\epsilon) &= 0 \\ D_T(\epsilon) &= 0 \end{aligned} \tag{B.13}$$

2. $\epsilon_1 < \epsilon_F < \epsilon_2$

$$\begin{aligned} n_T(\epsilon) &= \frac{V_T}{V_G}\frac{(\epsilon - \epsilon_1)^3}{\epsilon_{21}\epsilon_{31}\epsilon_{41}} \\ D_T(\epsilon) &= \frac{V_T}{V_G}\frac{3(\epsilon - \epsilon_1)^2}{\epsilon_{21}\epsilon_{31}\epsilon_{41}} \end{aligned} \tag{B.14}$$

3. $\epsilon_2 < \epsilon_F < \epsilon_3$

$$\begin{aligned} n_T(\epsilon) &= \frac{V_T}{V_G}\frac{1}{\epsilon_{31}\epsilon_{41}}\left[\epsilon_{21}^2 + 3\epsilon_{21}(\epsilon - \epsilon_2) + 3(\epsilon - \epsilon_2)^2 - \frac{\epsilon_{31} + \epsilon_{42}}{\epsilon_{32}\epsilon_{42}}(\epsilon - \epsilon_2)^3\right] \\ D_T(\epsilon) &= \frac{V_T}{V_G}\frac{1}{\epsilon_{31}\epsilon_{41}}\left[3\epsilon_{21} + 6(\epsilon - \epsilon_2) - 3\frac{\epsilon_{31} + \epsilon_{42}}{\epsilon_{32}\epsilon_{42}}(\epsilon - \epsilon_2)^2\right] \end{aligned} \tag{B.15}$$

4. $\epsilon_3 < \epsilon_F < \epsilon_4$

$$\begin{aligned} n_T(\epsilon) &= \frac{V_T}{V_G}\left(1 - \frac{(\epsilon_4 - \epsilon)^3}{\epsilon_{41}\epsilon_{42}\epsilon_{43}}\right) \\ D_T(\epsilon) &= \frac{V_T}{V_G}\frac{3(\epsilon_4 - \epsilon)^2}{\epsilon_{41}\epsilon_{42}\epsilon_{43}} \end{aligned} \tag{B.16}$$

5. $\epsilon_4 < \epsilon_F$

$$\begin{aligned} n_T(\epsilon) &= \frac{V_T}{V_G} \\ D_T(\epsilon) &= 0 \end{aligned} \tag{B.17}$$

Appendix C

Units

Among gaussian and SI and other unit systems, there are the so called *atomic units* (see also appendix 6 in [ZL83]), which are favored in atomic calculations. This term actually refer to two slightly different scalings. As in all unit systems, the fine-structure constant

$$\alpha = \frac{e^2}{4\pi\varepsilon_0\hbar c}$$

(here given in SI units) has to be conserved. For calculations on the atomic scale, the characteristic length is the Bohr radius

$$a_0 = \frac{4\pi\varepsilon_0\hbar^2}{me^2} = 5.29 \cdot 10^{-11}m,$$

while the Rydberg energy

$$Ry = \frac{\hbar^2}{2ma_0^2} = 13.61eV$$

is the typical energy dimension.

- For *Hartree units* you set

  $$\hbar = 1,\ m = 1,\ e = 1,\ \varepsilon_0 = \frac{1}{4\pi},\ c = \frac{1}{\alpha} \approx 137,$$

  with the result that lengths are given in Bohr radii, and energies are multiples of $2Ry$, which is called one *Hartree*. The kinetic operator takes the usual form

  $$\frac{\mathbf{p}^2}{2} \quad \text{or} \quad \frac{\mathbf{k}^2}{2}.$$

- In the *Rydberg* set you place

  $$\hbar = 1,\ m = \frac{1}{2},\ e^2 = 2,\ \varepsilon_0 = \frac{1}{4\pi},\ c = \frac{2}{\alpha} \approx 2 \cdot 137,$$

  resulting in lengths expressed in Bohr radii, and energies in multiple Rydbergs. But the kinetic operator takes the unnormal form

  $$\mathbf{p}^2 \quad \text{or} \quad \mathbf{k}^2.$$

Whichever of the two scalings you choose, you can just take a given gauss or SI formula and replace the quantities as mentioned above. The junction to the SI quantities energy, frequency and temperature is given by

$$\begin{aligned} 1\text{eV} &= 1.602 \cdot 10^{-19}\ \text{Ws} && \text{(C.1)} \\ \frac{1\text{meV}}{\hbar} &= 1.519\ \text{THz} && \text{(C.2)} \\ \frac{1\text{meV}}{k_B} &= 11.604\ \text{K}. && \text{(C.3)} \end{aligned}$$

Appendix D

Parameters of calculations

Electronic shells: The elements used in the calculations have the atomic configurations

Element	number	atomic levels
Al	13	[Ne].$3s^2.3p^1$
Ge	32	[Ar].$3d^{10}.4s^2.4p^2$
Ag	47	[Kr].$4d^{10}.5s^1$
In	49	[Kr].$4d^{10}.5s^2.5p^1$
Sn	50	[Kr].$4d^{10}.5s^2.5p^2$
Sb	51	[Kr].$4d^{10}.5s^2.5p^3$
Te	52	[Kr].$4d^{10}.5s^2.5p^4$
Au	79	[Xe].$4f^{14}.5d^{10}.6s^1$

basing on the noble elements:

Element	number	atomic levels
He	2	$1s^2$
Ne	10	[He].$2s^2.2p^6$
Ar	18	[Ne].$3s^2.3p^6$
Kr	36	[Ar].$3d^{10}.4s^2.4p^6$
Xe	54	[Kr].$4d^{10}.5s^2.5p^6$

This sections lists the most important parameters for the self-consistent FLAPW bulk calculations, which have been performed with the FLEUR code [FLE]. The space groups are given in XXX notation. The used exchange-correlation potential is the GGA approximation of XXX.

Test systems: These systems were calculated in chapter five for testing purposes. Aluminum was calculted in simple cubic configuration (sc) for two unit cells to illustrate backfolding.

Al sc		
lattice structure	sc	sc
space group		
inversion symmetry	yes	yes
atoms per unit cell	1	2
lattice parameters $[a_0]$	5.16	5.16, 10.32
$G_{max}[1/a_0]$	3.5	3.5
# of basis functions	110	206
# of electrons	3	6
# of k-points	6	6
local orbitals	no	no

It was calculated in the actual face-centered cubic (fcc) configuration as well to compare to literature.

Al fcc	
lattice structure	fcc
space group	
inversion symmetry	yes
atoms per unit cell	2
lattice parameters $[a_0]$	5.41, 7.67
$G_{max}[1/a_0]$	3.5
# of basis functions	184
# of electrons	6
# of k-points	6
local orbitals	no

The other test system was copper.

Cu	
lattice structure	fcc
space group	
inversion symmetry	yes

atoms per unit cell	2
lattice parameters $[a_0]$	5.41, 7.67
$G_{max}[1/a_0]$	3.5
# of basis functions	184
# of electrons	22
# of k-points	6
local orbitals	no

Germanium-Tellurium compounds: The cubic and trigonal phases were investigated:

GeTe cubic	
lattice structure	rocksalt
space group	
inversion symmetry	yes
atoms per unit cell	4
lattice parameters $[a_0]$	xx
$G_{max}[1/a_0]$	xx
# of basis functions	xx
# of electrons	20
# of k-points	xx
local orbitals	no

GeTe trigonal	
lattice structure	hexagonal
space group	
inversion symmetry	no
atoms per unit cell	6
lattice parameters $[a_0]$	xx
$G_{max}[1/a_0]$	xx
# of basis functions	xx
# of electrons	30
# of k-points	xx

local orbitals	no

Calcopyrites: The second class of systems investigated were Tellurium compounds in the calcopyrite structure.

AgInTe$_2$	
lattice structure	calcopyrite
space group	
inversion symmetry	yes
atoms per unit cell	8
lattice parameters $[a_0]$	xx
$G_{max}[1/a_0]$	xx
# of basis functions	xx
# of electrons	6
# of k-points	6
local orbitals	no

Bibliography

[BJA94] P. Blöchl, O. Jepsen, and O. K. Andersen. Improved tetrahedron method for brillouin-zone integrations. *Phys. Rev. B*, 49(23), 1994.

[Bro93] H. Bross. On the efficiency of different schemes for the evaluation of the density of states and related properties in solids. *phys. stat. sol. B*, 179, 1993.

[CC73] D. J. Chadi and M. L. Cohen. Special points in the brillouin zone. *Phys. Rev. B*, 8, 1973.

[Cun74] S. L. Cunningham. Special k-points in 2 dimensions. *Phys. Rev. B*, 10, 1974.

[Fer27] E. Fermi. *Atti Accad. Naz. Lincei, Cl. Sci. Fis. Mat. Nat. Rend*, 6, 1927.

[FLE] Fleur - full-potential linearized augmented plane-wave code of europe. `http://www.flapw.de`.

[GB75] G. Gilat and N. R. Bharatiya. Tetrahedron method of zone integration: Inclusion of matrix elements. *Phys. Rev. B*, 12, 1975.

[GR66] G. Gilat and L. J. Raubenheimer. Accurate numerical method for calculating frequency-distribution functions in solids. *Phys. Rev.*, 144, 1966.

[HK64] P. Hohenberg and W. Kohn. Inhomogeneous electron gas. *Phys. Rev.*, 1964.

[JA71] O. Jepsen and O. K. Andersen. The electronic structure of h.c.p. ytterbium. *Solid State Commun.*, 9, 1971.

[Koh85] W. Kohn. 1985.

[Kra] E. E. Krasovskii. *The ISOLDA manual, appendix B.*

[KSS99] E. E. Krasovskii, F. Starrost, and W. Schattke. Augmented fourier components method for constructing the crystal potential in self-consistent band-structure calculations. *Phys. Rev. B*, 59, 1999.

[Kur00] Ph. Kurz. *Non-Collinear Magnetism at Surfaces and in Ultrathin Films.* Forschungszentrum Juelich, Jül 3832, 2000.

[Lov89] D. R. Lovett. *Tensor properties of Crystals.* Adam Hilger, Bristol and New York, 1989.

[LT72] G. Lehmann and M. Taut. On the numerical calculation of the density of states and related properties. *Phys. Status Solidi B*, 54, 1972.

[Mad78] O. Madelung. *Introduction to Solid-State Theory.* Spinger Series in Solid-State Sciences. Spinger-Verlag, 1978.

[MPD] Ph. Mavropoulos, N. Papanikolaou, and P. H. Dederichs. A kkr green function formalism for ballistic transport. *Phys. Rev. B*, to be published, arXiv:cond-mat/0306604.

[Nye57] J. F. Nye. *Physical Properties of Crystals.* Oxford, 1957.

[RF75] J. Rath and A. J. Freeman. Generalized magnetic susceptibilities in metals: Application of the analytic tetrahedron linear energy method to sc. *Phys. Rev. B*, 11(6), 1975.

[Sin91] D. J. Singh. Ground-state properties of lanthanum: Treatment of extended-core states. *Phys. Rev. B*, 43, 1991.

[Sin94] D. J. Singh. *Planewaves, Pseudopotentials and the LAPW Method.* Kluwer Academic Publishers, 1994.

[Sla37] J. C. Slater. Wave functions in a periodic potential. *Phys. Rev.*, 51, 1937.

[Tho27] L. H. Thomas. *Proc. Cambrigde Philos. Soc.*, 23, 1927.

[YKS] O. V. Yazyev, K. N. Kudin, and G. E. Scuseria. Efficient algorithm for band connectivity resolution. *Phys. Rev. B*, 65.

[ZL83] P. Ziesche and G. Lehmann, editors. *Ergebnisse in der Elektronentheorie der Metalle.* Springer-Verlag, 1983.

Danksagung

- Krasovskij
- Aachen: Wuttig, Ralf, Wojtek